MCCXXII

UNIVERSITA' DEGLI STUDI DI PADOVA

Department of Industrial Engineering DII

MASTER OF SCIENCE IN AEROSPACE ENGINEERING

Design of a miniaturized hexapod rover for Martian exploration

Thesis advisor:

Prof. Stefano Debei

Thesis coordinator:

Ing. Sebastiano Chiodini

Candidate:

Irene Terlizzi

1234050

Academic Year 2021/2022

Abstract

The purpose of this work is the preliminary design of a miniaturized bio-insipired hexapod robot for the exploration of Martian lava tubes, i.e. the underground conduits formed through the lava activity of non-explosive volcanoes. For this purpose, a suite of sensor was chosen for the characterization of these environments. With the aim of mapping the caves, the hexapod has been equipped with a camera and a series of sensors were also identified to measure the presence of perchlorate, the dose of radiation that passes the basaltic layer, the temperature and the relative humidity inside the lava tubes. In this work, the reasons for choosing this type of analysis are also explained, along with the identified instruments. The choice of sensors to accommodate in the hexapod led to have the preliminary dimensions of the robot, so that a decision could be made on the configuration. The configuration chosen consists of a rectangular central body with the six legs arranged symmetrically along the longest side, the legs were designed based on those of insects. Being an initial design, it was used the simplest configuration to verify the components and the possible realisation of it. The robot was reproduced using Solidworks and then imported in Simulink. The main chapter is focused on the simulation of the robot and its motion through the MATLAB&Simulink environment so that the possibility of using the smallest servos found on the market can be verified, through the sensing of the torques required by the rover. The inverse kinematics method was used to impose a semi-elliptical trajectory on the legs through dedicated scripts and functions that create the vectors of the position profiles, the velocity profiles and finally the vectors of the acceleration profiles that have been set trapezoidal to avoid problems due to discontinuity. Three types of gaits were tested: metachronal, ripple and tripod gait, corresponding to three speeds of the robot. It was possible to verify the use of servos through modelling, as the limits imposed by them were respected.

Index

List of figures

List of tables

Chapter 1

Introduction

Bio inspired robots are a category of robots characterized, as the name says, by an architecture based on the structure of biological system, because optimized for the survival in their precise habitat.

The first studies inspired on the gait of biological beings were based on the observation of various type of animals and nowadays this kind of research observation are still done in an effort to replicate their motion pattern. [1]

Among the categories of this type of robots it is possible to find the terrestrial legged, identified by the presence of two legs (bipeds), four legs (quadrupeds), six legs (hexapods) or eight legs (octopods).

Multi-legged robots require more effort in controlling their motion due to their high complexity caused by the numerous actuators as each leg need at least three of them, which lead to a large power consumption and a low energy efficiency. [1]

Their attractivity, compared to the wheeled ones, is in their versatility, considering that missions usually take place in remote locations and difficult environment like seabed, planets or search and rescue operations. Legged robotd can walk on uneven terrains where the wheeled can't and they can climb bigger obstacles because of the absence of the wheels which put a stricter limits on their size: specifically, the size of a obstacle must be half of the diameter of the wheel, opposed to constrains of the leg where the length of it must be comparable with the size of the leg.[2] Moreover, the wheeled are more likely to damage terrain in situation where the aim is the analysis of the ground.

For the purpose of this study, it has been chosen to implement a robot moved by six legs for many reasons. Hexapods can be found between insects and there are a various number of gaits type one can consider some of whom will be discussed in chapter 3.

Also, to maintain the balance of the robot are required only three legs but to implement the movement in a stable way are needed at least four legs, so hexapods show great agility in walking and redundancy because in case of failure of two legs the robot can continue his mission. The six legs allow the robot, in addition to being more reliable, to have better walking performance than those with fewer legs, as when the robot is walking, stability decreases during the leg transfer phase.[1,2]

Many hexapod rovers for space exploration have been designed and built in the last years thanks to the development of control system technology, all of them equipped with various sensing system in pursuit of their main missions.

Table 1 displays a series (not all) of hexapods developed in the last twenty years, although the masses in this table are deliberately limited to 27 kg (except LAURON V), this gives an idea of how large the research, and the state of art are.[3]

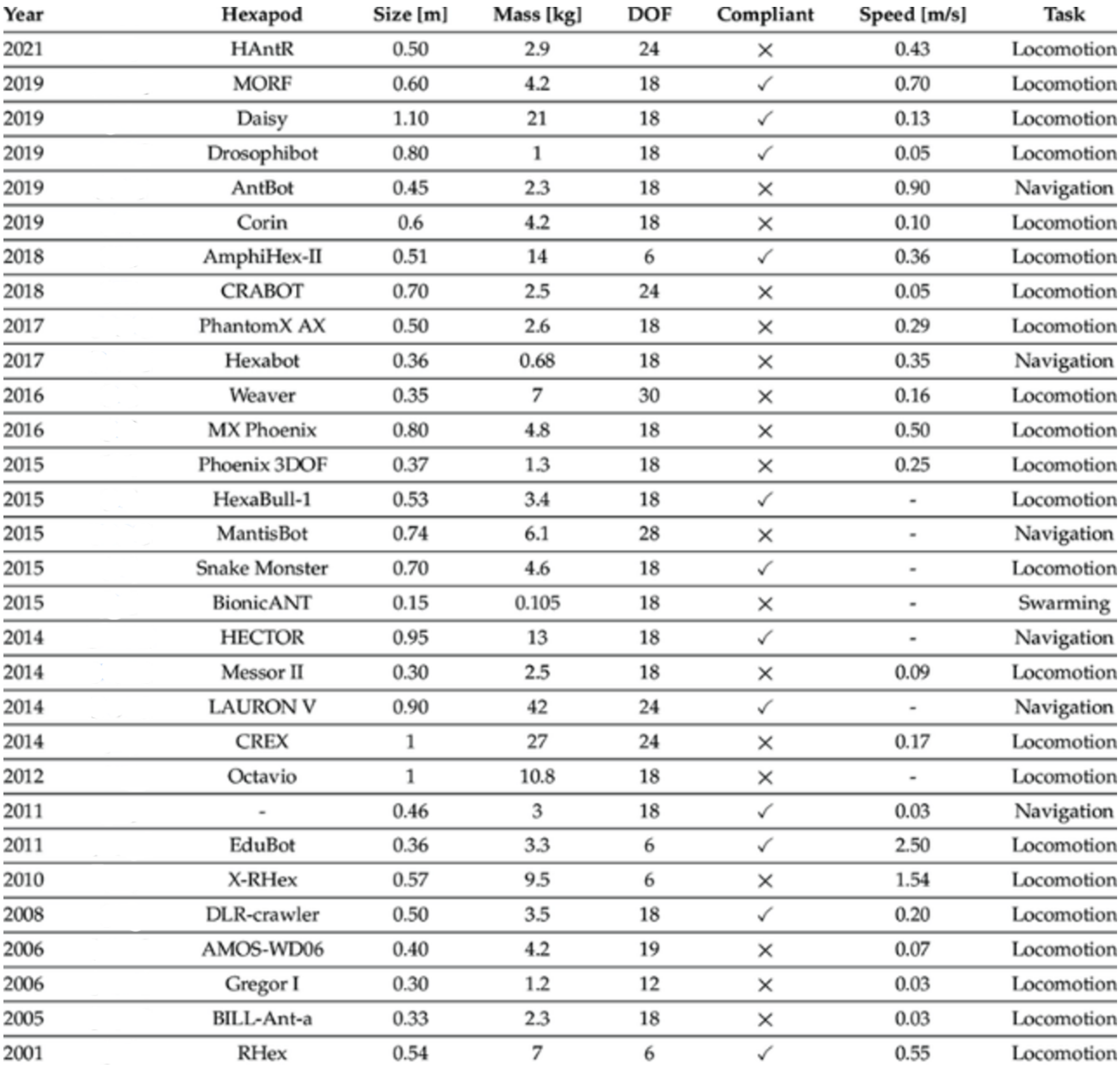

Year	Hexapod	Size [m]	Mass [kg]	DOF	Compliant	Speed [m/s]	Task
2021	HAntR	0.50	2.9	24	×	0.43	Locomotion
2019	MORF	0.60	4.2	18	✓	0.70	Locomotion
2019	Daisy	1.10	21	18	✓	0.13	Locomotion
2019	Drosophibot	0.80	1	18	✓	0.05	Locomotion
2019	AntBot	0.45	2.3	18	×	0.90	Navigation
2019	Corin	0.6	4.2	18	×	0.10	Locomotion
2018	AmphiHex-II	0.51	14	6	✓	0.36	Locomotion
2018	CRABOT	0.70	2.5	24	×	0.05	Locomotion
2017	PhantomX AX	0.50	2.6	18	×	0.29	Locomotion
2017	Hexabot	0.36	0.68	18	×	0.35	Navigation
2016	Weaver	0.35	7	30	×	0.16	Locomotion
2016	MX Phoenix	0.80	4.8	18	×	0.50	Locomotion
2015	Phoenix 3DOF	0.37	1.3	18	×	0.25	Locomotion
2015	HexaBull-1	0.53	3.4	18	✓	-	Locomotion
2015	MantisBot	0.74	6.1	28	×	-	Navigation
2015	Snake Monster	0.70	4.6	18	✓	-	Locomotion
2015	BionicANT	0.15	0.105	18	×	-	Swarming
2014	HECTOR	0.95	13	18	✓	-	Navigation
2014	Messor II	0.30	2.5	18	×	0.09	Locomotion
2014	LAURON V	0.90	42	24	✓	-	Navigation
2014	CREX	1	27	24	×	0.17	Locomotion
2012	Octavio	1	10.8	18	×	-	Locomotion
2011	-	0.46	3	18	✓	0.03	Navigation
2011	EduBot	0.36	3.3	6	✓	2.50	Locomotion
2010	X-RHex	0.57	9.5	6	×	1.54	Locomotion
2008	DLR-crawler	0.50	3.5	18	✓	0.20	Locomotion
2006	AMOS-WD06	0.40	4.2	19	×	0.07	Locomotion
2006	Gregor I	0.30	1.2	12	×	0.03	Locomotion
2005	BILL-Ant-a	0.33	2.3	18	×	0.03	Locomotion
2001	RHex	0.54	7	6	✓	0.55	Locomotion

Table 1: *Overview of the state-of-the-art hexapod robots developed over the last 20 years in the range 1/27 kg. The size, given in meters, corresponds to the largest dimension between width and height.*

The system was designed with the goal of exploring confined spaces where the slope of the terrain and its characteristics are completely unknown.

The purpose of this work is to design a hexapod robot with its equipment by miniaturizing it as much as possible. Then after the design phase, verify the torques required for movement in order to use the servos found, which turn out to be the smallest on the market, so that it is able to carry out its mission moving around the environment and analysing it thanks to the sensors it was equipped with, which will be described in chapter 2.

Compared to *Table 1* above, the robot in this work resulted smaller in size as it is 0.12 m, and the mass is in the lower ranges of the table as it is about 0.23 kg. Its DoF are 18 which are the minimum required for a hexapod to move. Its average speed is 0.00075 m/s so two orders of magnitude lower than the lower speed in the table. The robot is comparable to the dimensions of the BionicANT but the average speed of this model is not given, since it can be seen from the table that there is no linear relationship between speed and dimensions it is not guaranteed that the speed of the robot in this work is comparable with that of the BionicANT.

1.1 Lava tubes

As the robot mission was conceived as a Martian exploration mission, it is appropriate to call it a rover.

In particular, the rover will not explore and investigate the outer surface of the Red Planet, but its research sites will be the lava tubes, also called pyroducts.

Lava tubes are caves created by a low viscosity basaltic lava flows from a non-explosive volcano, when the outer surfaces of lava channels cool more rapidly compared to the core, this process forms a crust with an empty tube coated with lava on floors, walls, and ceiling.

The outer surface of the lava flow solidifies faster than the inner surface as it exchanges heat with the surface, which is at a lower temperature. In this way the surface becomes more and more viscous until it becomes completely solid, isolating the lava inside.[4–6]

Lava tubes are in most cases sub-parallel to the surface. The cross-section of lava tubes is usually arched, round, oval or keyhole-shaped, due to lava growth on the side walls and lowering caused by thermal erosion as in *fig.1.1*.[6]

On Earth, we can observe the presence of these lava tubes in various volcanic areas as USA (Kilauea Volcano in Hawaii), Italy (Mount Etna), Australia (Undara Volcano), Iceland, the Canary Islands, Azores, India, Vietnam, Korea, Japan, Galapagos Islands, Easter Island, Mexico, Kenya, Saudi Arabia and Jordan.[7] Their morphological characteristics on Earth are studied and well know: their length vary from a few meters to tens of kilometres while their width and height go from 0.5 m up to a few dozen of meters, with a slope superior to 4°.[4,6]

Figure 1.1: *Thurston lava tube, Hawaii Volcanoes National Park, Big Island of Hawaii, U.S.A. - Michael Oswald*

As regards Martian lava tubes the related flow features are not as well known, they were first recognized based on Viking orbiter images and have since then been identified using orbiter imagery from Mars Odyssey (MO), Mars Global Surveyor (MGS), Mars Express (ME), and Mars Reconnaissance Orbiter (MRO) as the one in *fig.1.2.* On Pavonis and Ascraeus Montes, as well as in flows from Hadriaca Patera, lava tubes appear to be collapsed, leaving linear, sometimes discontinuous, channel-like features.[5]

These tubes have also been identified mainly by the presence of skylights, which are openings formed when a section of the ceiling collapses. Thanks to visible and thermal orbiter images were spotted skylights in Arsia Mons region with a diameter of 100 to 250 m. Is to be said not all skylights formed in volcanic terrains, they could be consequences of an impact melts, and as in these cases other processes could be responsible for their formation [6]

Because of the relatively recent discovery of the caves and because they were identified by orbiters, the morphological characteristics of Martian lava tubes remain fairly unknown. Considering the lower Martian gravity, which is almost 0.38 of Earth's gravity, it is fair to take into account the formation of larger underground caves caused by the passing of lava, this means also having larger skylights and tubes which may be greater than one order of magnitude compared to the terrestrial ones.[6]

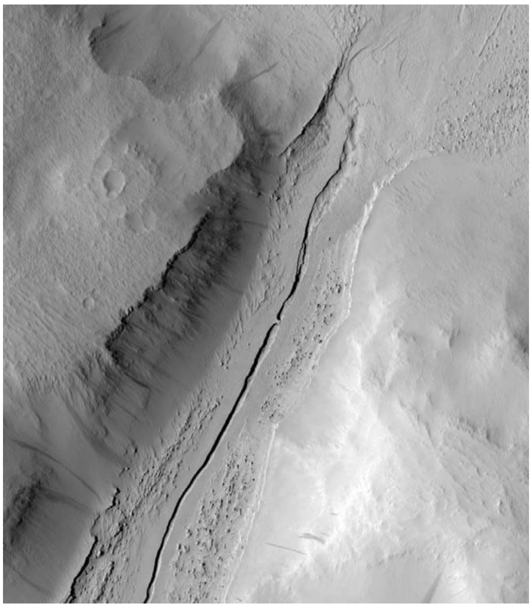

Figure 1.2: *Portion of MRO/HiRiSE image of a channel-like conduit in Tartarus Colles. Credit: NASA/JPL/University of Arizona*

The possibility of their large dimensions is appealing because they could provide the ideal space for a possible settlement which would be the solution for some of the issues of Mars' habitability:

- *Dust shielding:* Mars is a highly oxidising environment, rich in peroxides that pose a hazard to humans. Due to the low gravity, compared to the Earth, and to the less dense atmosphere, dust particles raised during storms and dust devils tend to move more and stay longer in the atmosphere, these particles also can be less than 5 μm in size. For this reason, they are a danger, not only to machinery, but mostly to humans, as exposure to these dusts can cause respiratory problems. For this very reason air filtering in caves is a benefit.[4]
- *Avoidance of meteoric impact:* Also due to its atmosphere, Mars is proven to have a larger probability to have a meteoric impact large enough to create a small crater, in this case the basalt over the caves could provide protection.[4]
- *Controlled temperature variations:* Mean annual surface temperatures are approximately 215 K at the equator and 160 K at the poles;[5]
  The temperature gradient between the day side and the night side is also important, mostly since the greenhouse effect on Mars is not strong.[8]
- *Radiation shielding*: lava tubes would provide protection from ultraviolet radiation ad cosmic rays. The first will be blocked by the basaltic ceiling the second ones require analysis in situ which will be discussed in chapter 2.2.2.

On the other hand, the exploration will have to take into account the communication problems resulting from being underground and the decreasing, if not absent, solar power needed to recharge the battery of the rover.

As stated the aim of this work is therefore to present an initial design of a hexapod rover, with an initial analysis of its movement, which will be tasked with entering lava tubes to map their evolution on the planet and collect data on their environmental conditions such as the presence of oxidants, the amount of radiation penetrating the basalt and the climatic conditions, such as temperature and relative humidity.

In chapter 2, the architecture chosen for the rover will be explained, with a focus on the type of analysis to be carried out and the sensors used for this. In particular there will be a brief introduction on perchlorates and when and how they were detected and subsequently it will be explained how it was intended to search for them; also, cosmic rays will be taken into account as another relevant field of research to habitability.

In choosing the rover's architecture, an attempt was made to minimise the system as much as possible so that it could move and explore confined spaces which is the main task of the rover.

Chapter 3 deals with the kinematic and dynamics of the rover, the equations of direct and inverse kinematics and the results of comparisons of various types of gaits, obtained from modelling in the MATLAB&Simulink environment with the aim of verifying the possibility of using the chosen actuators that will be presented together with the sensors.

Chapter 2

Rover s design

This chapter introduces some of the various configurations that a walking hexapod can assume, with an overview on the one chosen presented with his CAD model. The second part of the chapter deals with the scientific purposes that led to the development of this design.

2.1 Architecture

Hexapods walkers are a category of the bio inspired robots, this type of robot has an architecture based on the constitution of biological beings, especially regarding the leg structure and movement. This inspiration has numerous levels, from the disposition of the legs to the orientation to the component of one single leg.
First of all, a distinction must be made between two basic architectures of hexapod robots: rectangular, where the robot has its legs distributed symmetrically along the two sides, and hexagonal with the legs distributed axially-symmetrically around the body with a hexagonal or circular form so that any direction can be used as the forward direction. on the contrary, rectangular robots require a particular command in order to turn, which will be discussed in the next chapter as it is the architecture chosen for the hexapod in this work. [2]
Although the literature shows a circular configuration to be more advantageous, the choice fell on the rectangular one primarily because the internal space could be better distributed, as all components are rectangular in shape, and secondly because it was easier in preliminary simulations to distinguish the hierarchy of the legs and identify the problems of each one.
A further distinction derives from the choice of whether or not to be inspired by biological beings, having bio inspired robots or non-zoomorphic ones. After choosing the former, the choice of leg configuration is based on three main categories: mammals, reptiles, arachnids.[2]
As shown in *fig.2.1* mammals are characterised by the fact that their body sits on top of their legs requiring more stability but less energy to support the body.

Reptiles, on the other hand, have legs protruding from the body with the ends of their knees lying to the side, as opposed to arachnids, which instead have the ends of their knees on top of the main body. [2]

Aside from the circular leg configuration, which regards the hexagonal architecture, the rectangular one has two main ways of orienting the legs: frontal, where the robot advances perpendicular to the movement of the legs, and sagittal where the direction of advancement is instead parallel.[2]

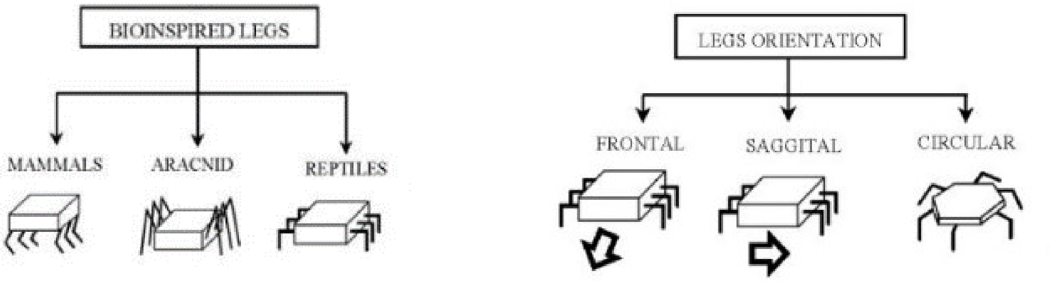

Figure 2.1: *Type setting of hexapod legs' design.*

In this work, the arachnid configuration was chosen because it has a lower centre of gravity with the same size of the legs compared to the reptilian, and in order not to put all the weight of the main body on the knees as with the mammals, as the torque limits of the actuators are a bit strict. The legs are positioned symmetrically on both sides at a distance of 20 mm; it is easy to switch to the reptilian configuration by changing the initial conditions for kinematics, which will be discussed in the next chapter.

Having chosen the arrangement and orientation of the legs, the next step is the modelling of the components of each leg. Based on the legs of an insect, each is generally made of five basic elements connected by joints, meaning one leg has 5 DoF (degree of freedom), these segments are Coxa, Trochanter, Femur, Tibia and Tarsus as depicted in *fig.2.2.*

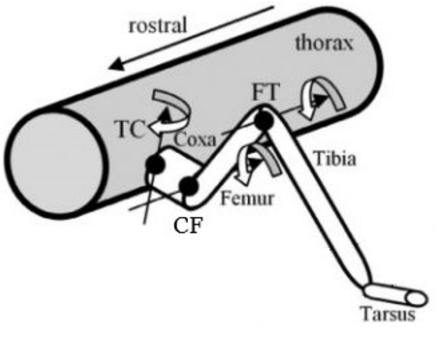

Figure 2.2: *A scheme of a typical stick insect leg*

Usually 3 DoF mechanisms are implemented, as the remaining two degrees of freedom are considered unnecessary for a standard walking process, thus having six legs will result in the hexapod having 18 DoF.

Therefore, following the above analogy, within the leg mechanism can be distinguished three parts with their respective degrees of freedom: Coxa, Femur and Tibia.[1,9]

The Coxa, through the TC joint is connected to the main body by a revolute pair of vertical direction that is responsible for forward and backward movement of the leg, and it is called the *base joint*. The Femur is connected to the other end of the Coxa via a horizontal revolute pair, and it is responsible for lifting the leg with the CF joint called the *hip joint*. The other end of the Femur connects to the Tibia via the FT joint, called the *knee joint*, which allows extension and flexion of the tibia via a horizontal revolute pair. The Tibia is responsible for supporting the leg and as the other end is in contact with the ground and through friction allows the robot to move in the space. [1,9,10]

The mechanical design of the robot focuses on two main components: the body and the legs. It was done through a CAD model made with the Solidworks program and then imported into the Simulink environment via the *Simscape Multibody link* extension

The body of the robot has the function of housing the electronic circuits, the battery, the various sensors, and it serves as a link between all the legs which are symmetrically distributed along the body. A rectangular case was modelled consisting of a lower base and an upper lid held together by eight screws. The case once assembled is 120 x 70 x 30 mm^3 with a thickness of 3 mm; these dimensions were verified preliminarily, through the CAD model in *fig.2.3,* that

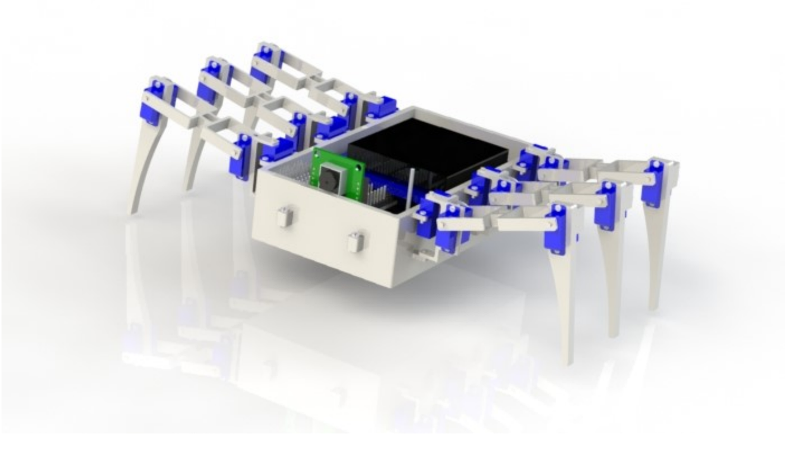

Figure 2.3: *Model used to verify geometric requirements of instruments*

allow to equip the rover with all the tools it may need while maintaining compact dimensions, having found ones consistent to the geometrical requirements.

The legs were designed precisely following the configuration described above, so with three parts each with a dedicated space for the placement of the servos that will serve as TC, CF, and FT joints.

The CAD model of the Coxa, Femur and Tibia and of the entire leg is shown in *fig.2.4*.

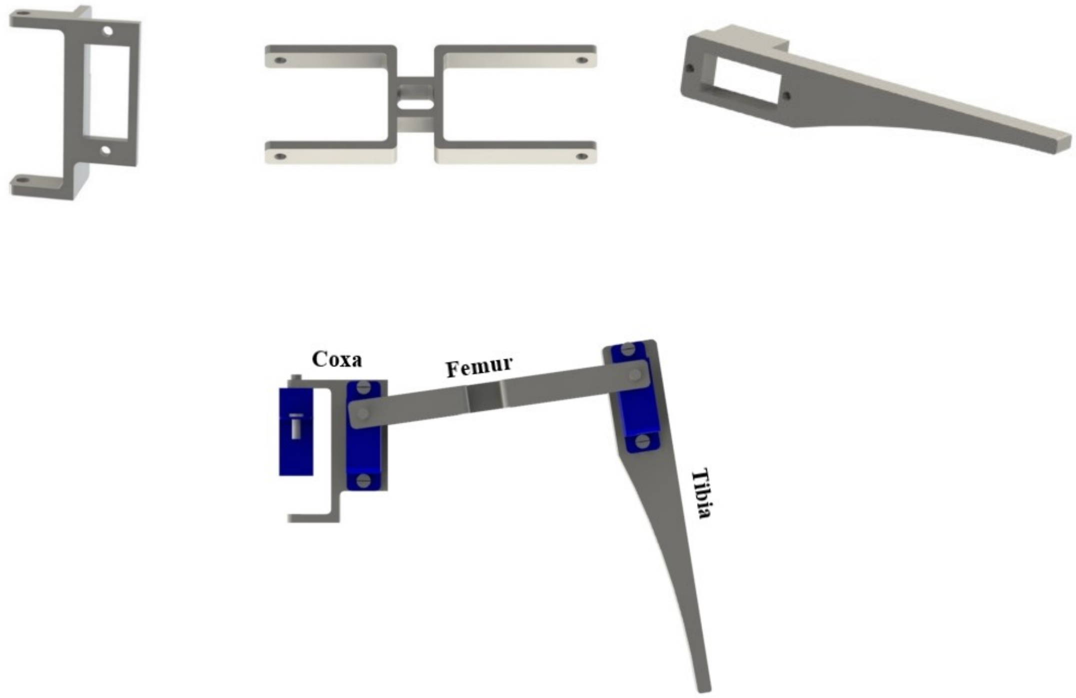

Figure 2.4: *CAD model of the pieces of the leg and of the leg assembled*

According to the size of the case the legs were designed to make it possible to move the main body and to keep it at a certain height from the ground, from literature it was seen that the shortest part is the Coxa while the Femur and Tibia are comparable in length. *Table 2* shows the lengths of the components, measured from the connection with the preceding piece to the connection with the next piece. The preceding piece is considered the case for the Coxa, while in the case of the Tibia the successive is the ground.

Leg part	*Length (mm)*
Coxa	12.30
Femur	49
Tibia	58.70

Table 2: Measures of the component of the leg CAD model

In the simulation, a density of 2690 kg/m^3 was imposed to the elements that constitute the legs and the main body of the rover. This value corresponds to the density of alloy AA 6082 an alloy of the aluminium-magnesium-silicon family, frequently used for applications where good strength values, good corrosion resistance and good machinability are required.[11]

By imposing this density on the volumes automatically computed by Solidworks and considering the mass of the servos, given in the datasheet, that will be presented in the next chapter, resulted in a rover with a mass, net of the instruments with which it was equipped, of 0.228 kg.

Fig 2.5 shows the CAD model imported into Simulink to simulate the movements of the rover.

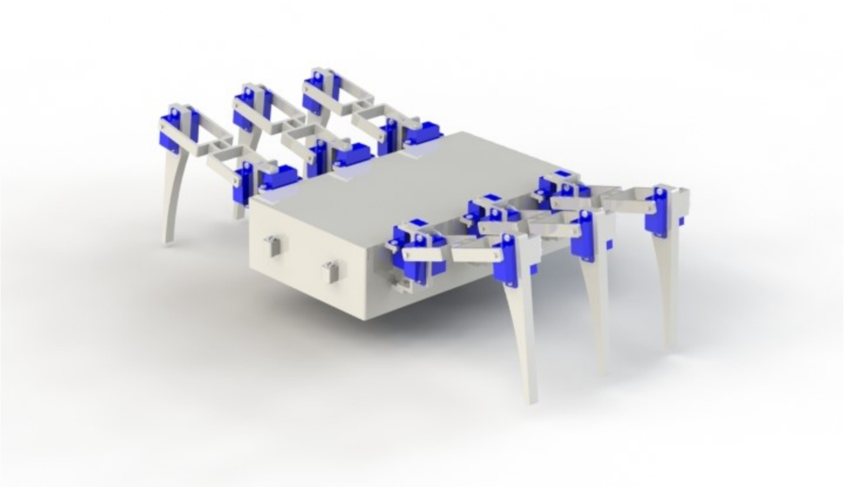

Figure 2.5: *Model imported into Simulink environment*

Besides the sensors necessary to the analysis and to the movement, the rover has been equipped with the board *Arduino Nano*, based on the microcontroller *ATmega328,* with 22 digital I/O pins which will be responsible for receiving information from the motion sensors, analysing it and processing the commands for the servos. His dimensions are very compact as it measures 18 x 45 mm^2 and weights of 7g.

Due to the large number of servos to be controlled, it was decided to use a servo driver. The *Adafruit 16-Channel 12-bit PWM/Servo Driver* was chosen, which is capable of providing 16 distinct PWM (pulse width modulation) control. The PWM/Servo Driver uses I^{2}C so it takes only 4 wires to connect to Arduino.[12]

Since 18 servos are required for the motion, two servo drivers will have to be chained in order to control them all separately, the remaining unconnected pin can be used for other purpose like for example to connect the led the rover will need to light the tubes. In terms of dimensions each board measures 62.5 x 25.4 x 3 mm^3 and weighs 9g, pin included.

Although they are micro servos, their number and the need for a holding torque when not in motion, require the use of a battery with sufficient capacity to power all 18 of them all the time, so was considered in the body a space for a 3000 mAh LiPo rechargeable battery.

Finally, a telecommunication module was planned, in this case the *XBee-PRO S2C* with an indoor range of 90 m and an outdoor range of 3200 m.

With all the components the robot has been equipped and all the cables and electronics, the total mass is estimated to be around 0.2853 kg.

2.2 Science requirements

The main target of the rover as it has been conceived is the underground exploration of Martian lava tubes. In addition to the mapping of these channels and the estimation of their size, other analysis targets have been considered as interesting fields for the investigation of these.
Here we present the reasons it has been chosen to carry out these analyses and the instruments identified that satisfied the requirements, summarized in *Table 3*.

Field of analysis	*Type of analysis*	*Instrument*	*Accuracy*
Perchlorate	Presence	NIR spectrometer	-
Cosmic Rays	Amount	Muon Detector	± 1 ms
Temperature	Diurnal/Seasonal variations	Temperature sensor	± 1 K
Relative Humidity	Diurnal/Seasonal variations	Relative Humidity sensor	± 5 %

Table 3: Summary of the analysis to be carried out

2.2.1 Perchlorate

Mars is a strong oxidising environment, rich in perchlorate which is considered stable at Martian temperature.[13]
The perchlorate ion, with the chemical formula ClO_4^- is the anion of chlorine with oxidation state +7.

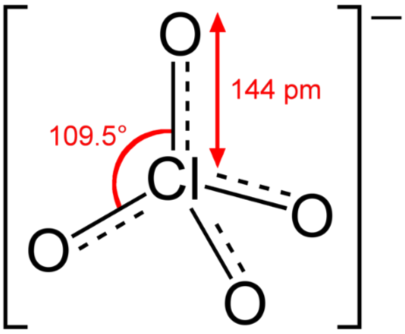

Figure 2.6: *Model of perchlorate ion*

The undeniable identification of the perchlorate ion is owed to Phoenix which was equipped with an instrument belonging to the Wet Chemistry Laboratories (WCLs), part of the Microscopy, Electrochemistry, and Conductivity Analyzer (MECA) package, with two selective electrodes: the first one was originally intended as nitrate sensor (Hofmeister sensor) , but turned out to be three orders of magnitude more sensitive to perchlorate than nitrate and the second one for calcium (Ca^{2+}) detection which was only responsive to perchlorate because was the only anions causing an interference in its response to Ca^{2+}. Thanks to these two sensors was measured a concentration of 0.6 wt.% of ClO_4^- in the soil, which is a significant amount compared with Earth were typical concentrations are three to four orders of magnitude lower.[14,15]

The presence was then confirmed by a release of oxygen from heating the samples which was interpreted as a result of perchlorate breakdown.

Further to this finding also Viking data were reinterpreted as consistent with the presence of perchlorate.

Eventually with the Sample Analysis ad Mars (SAM) instrument on Curiosity rover an evolved gas analysis (EGA) was made on a soil sample resulting in a detection of O_2 and chlorinated hydrocarbons which worked as validation of an oxychloride phase, like perchlorate, in the ground.

In the end with the discoveries of perchlorate from Phoenix and Curiosity, as well as evidence of oxidants at both Viking sites, it was possible to affirm the hypothesis that ClO_4^- was ubiquitous on Mars.[14,16]

After obtaining evidence of the perchlorates in the Martian regolith, it still remains to be established what compounds it is part of. It is safe to assume that it occurs in the soil in the form of perchlorate salts of K^+, Na^+, $Ca^{2+,}$ $Mg^{2+,}$ Fe^{2+}, Fe^{3+}, and Al^{3+}. Indeed, subsequent WLC's data reanalysis support the presence of $Ca\ (ClO_4)_2$ as predominant in the soil.[13] Perchlorate salts are highly soluble in water and the ClO_4^- ion is kinetically inert upon reduction and tends to be absorbed into minerals or organic surfaces, making it very persistent in the environment.[15]

The importance of the presence of such concentration of perchlorate in the soil lies in the fact that firstly it is a health concerns because it is highly toxic and can affect the functioning of the thyroid preventing the absorption of iodine in human body, causing hypothyroidism and neuroglial dysfunction.[15,17] Moreover ionizing radiation is able to decompose the perchlorate into other chloride oxidations forms like ClO_2^- and ClO^- which are much more reactive and can cause other types of health problems like breathing difficulties, headaches, skin burns, loss of consciousness and vomiting. These species can also be a concern because of their corrosive power.[15]

The main way in which astronaut could be exposed to perchlorate is through inhalation of dust mostly during dust storms where particles of all size would be blown up.

In particular, inhalation of dust particles <5 µm is the major problem because the lung mucus can't expel particles too small; taking into account the concentration of perchlorate in regolith a few milligrams of inhaled dust particles would already exceed the RfD.[15] (Reference dose)

The interest in the presence of perchlorate on Martian soil is linked to other factors besides the reason just mentioned: firstly, it could be evidence of the existence of Martian life as ClO_4^- can be used as a terminal electron acceptor by a variety of prokaryote, secondly being a freezing point depressant, it could allow the formation of brines, and since perchlorates are highly deliquescent (i.e. they have a tendency to transform from a crystalline solid to an aqueous state under humid conditions) these compounds could represent a potential for the presence of H_2O on the surface under environmental conditions such as those on Mars.[13]

Finally, the most beneficial use of ClO_4^- on Mars would be as a source of oxygen, considering that on average humans breathe or consume about 550 litres of oxygen per day. Based on the amounts of ClO_4^- measured in the Martian regolith, a daily supply of oxygen for an astronaut could be achieved by the complete dissociation of ClO_4^- contained in regolith.[14,15]

The analysis of the presence of perchlorate was based on the results of the paper [13] where K^+, Na^+, Ca^{2+}, Mg^{2+}, Fe^{2+}, Fe^{3+}, and Al^{3+} perchlorate salts were studied to provide spectral and thermal data for detecting and characterizing their possible presence on Mars.

After the study it was found that near-infrared (NIR) spectral features for perchlorates are dominated by H_2O bands that occur at 0.978–1.01, 1.17–1.19, 1.42–1.48, 1.93–1.99, and 2.40–2.45 µm.

On the basis of these data the sensor considered for analysing the occurrence of the perchlorate compounds in lava tubes is a NIR mini spectrometer.

The spectrometer is the *Pebble NIR* of Ibsen photonics equipped with a sensitive un-cooled G13913 InGaAs (Indium gallium arsenide) detector from Hamamatsu., designed specifically for portable analytical instruments.

The spectral response range is 950 to 1700 µm and offers a resolution of 12 nm so the instrument is capable to detect three ranges where the peaks of the salts are present as referred in *fig.2.7.*

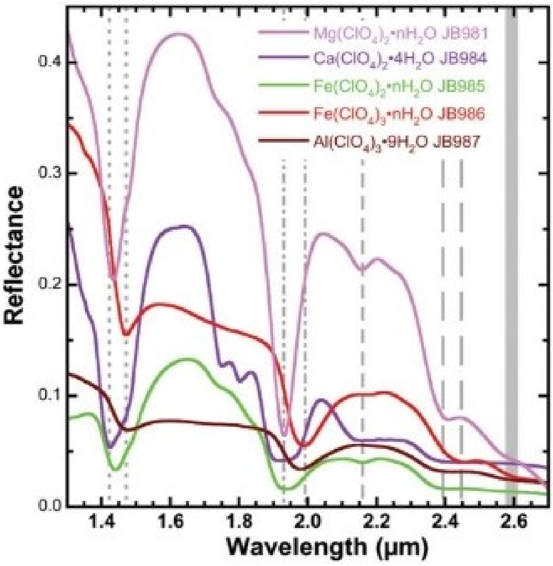

Figure 2.7: *NIR reflectance spectra from 1.2–2.7 µm. The Mg perchlorate spectrum has a much brighter reflectance in this region and is divided by 2 for this plot.*

This analysis only serves to sense the presence of the compound and if so, how deep it goes in the pyroducts, for a concentration analysis other instruments are needed, but since the study of perchlorate on Mars is relatively new this first analysis is intended to provide initial data on where to investigate.

Figure 2.8: *Pebble NIR spectrometer*

2.2.2 Cosmic Rays

Mars is known having no magnetic field, this and the thinner (<1%) Martian atmosphere compared to the Earth's one result in a much stronger exposure to radiation because of the lack of shielding against high-energy particles impacting on it, which interact with the atmosphere and if their energy is high enough, they penetrate several meters in the Martian regolith resulting in producing secondary particles. [18]

A popular acronym for highly energetic charged ions is HZE, as these particles do not make it to the Earth's surface, terrestrial life has not evolved mechanisms to deal with the complex DNA damage that can be caused by the crossing of an energetic heavy ion. HZE particles consequently present a health risk to humans, who will receive chronic exposures whose effects include the possible manifestation of acute radiation syndrome effects such as nausea, emesis, haemorrhage or possibly even death. The large organ dose-equivalents associated with these events 0may also contribute significantly to an increased risk of cancer induction and mortality in the spacecraft crew. [19,20]

It is possible to split the source of the permanent higher ionizing radiation (IoR) two main causes: the firsts are the galactic cosmic rays (GCRs), the seconds are the solar energetic particles (SEPs). [21]

GCRs are high-energy particles whose energy span from 10 MeV/nuc to 10 GeV/nuc linked to the most energetic events and active objects in the Universe like supernovae explosions, pulsars, active galactic nuclei, relativistic jets.[18,22] Their composition varies slightly with time but in general there is 87% H-ions, 11% He-ions (α particles), electrons ~1%, and ~1% heavier nuclei. [18,19,21]

The composition of SEPs instead is highly variable, generally dominated by protons, as they are produced in the solar corona by high-energy processes associated with flares, coronal mass ejections (CMEs), and their corresponding shocks. Their onset times, their duration and their magnitude are difficult to predict as they vary several orders of magnitude, as an example their mean duration is of 4,13 days but they can last from a few hours up to a week. [18,21]

GCR flux decreases during solar activity maximum and increases during its minimum, instead the risk for exposure to SEPs increases with solar activity. Thus, the contribution of each to the total mission dose of a future mission on Mars depends on when the mission takes place. [18]

Radiation dose, D, is defined to be the energy deposited per unit mass in water the unit is the Gray (J/kg = m^2/s^2). The practical measure is of radiation exposure is not dose, but dose-equivalent, given in units of Seiverts (J/kg = m^2/s^2) and attempts to account for the varying biological effects of different types of radiation, by assigning a quality factor Q.[19]

Data concerning the radiation dose or dose-equivalent on Mars surface are several starting from HZETRN (High charge (Z) and Energy TRaNsport) which is NASA-JSC a deterministic space radiation transport code that can calculate the GCR flux at various points in the solar system, as the effect of shielding. Considering as only shielding the Martian atmosphere HZETRN has computed a value of dose in the range between 200 to 300 mSv/yr, since the atmosphere's thickness vary with altitude. [19]

There have been in situ measurements with MARIE (Mars Radiation Environment Experiment) one of three science instruments aboard the 2001 Mars Odyssey spacecraft whose purpose was the measurement of the radiation environment on the planet, analysing GCRs and SEPs, to provide useful information for future manned missions.

MARIE orbiting recorded a GCR dose about 250 mGy/d corresponding to 300 or 400 mSv/yr depending on Q. In measuring a SEP, the instrument showed that the dose reached a peak of about 10 mGy/d, 30 mGy for the total event, since the event was dominated by protons implying and average value of Q close to one the dose equivalent of the event was about 30 mSv, comparable to a full month exposure to the GCR. [19]

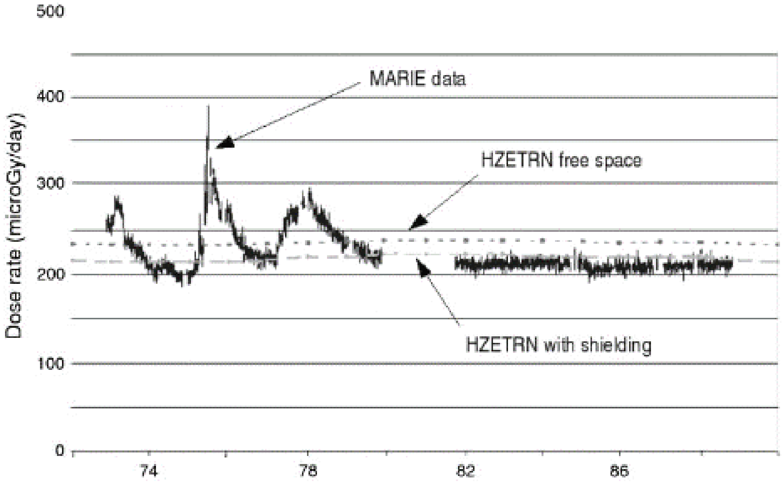

Figure 2.9: *Radiation dose-rate at Mars as measured by MARIE and as calculated using HZETRN for March 2002*

A more accurate estimation of the radiative environment is due to the Radiation Assessment Detector (RAD) on the Mars Science Laboratory's (MSL) Curiosity rover which started making detailed measurements of the cosmic ray and energetic particle radiation environment on the surface of Mars in 2012, resulting the diurnal dose rate vary between 180 and 225 mGy/d due to the variation in Mars environment during the day.[18]

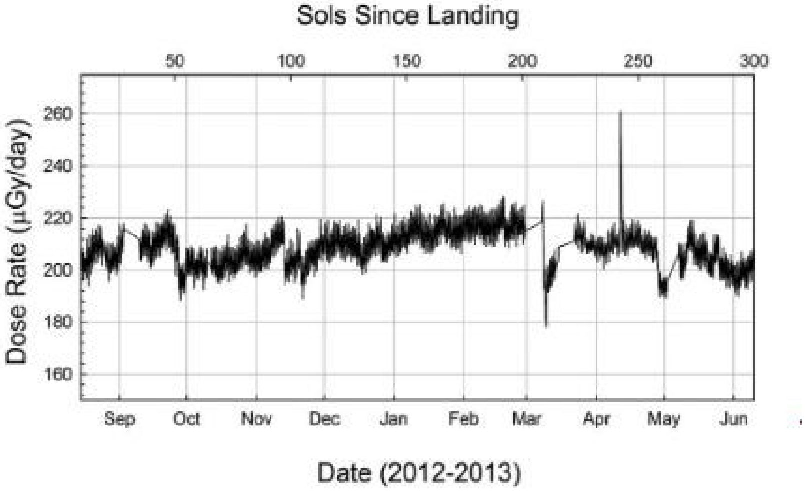

Figure 2.10: *Time series of radiation dose rate measured by RAD on the surface of Mars.*

For comparison, cosmic rays entering Earth's atmosphere give a dose equivalent from 260 μSv/yr, at sea level, to 500 μSv/yr, a factor of 1000 lower [19]

Various studies have tried to model the expected radiation regime underground, but the dose values were dependent on the modelled radiation environment at the surface, which is why it was decided to analyse the radiative environment inside the lava tubes. By having an idea of how far the radiation penetrates the basalt, it will be possible to understand whether these caves could be the solution to the problem of high exposure to Martian radiation in view of a possible settlement.[18]

The instrument chosen to equip the rover is the CosmicWatch Muon Detector.

CosmicWatch is a Massachusetts Institute of Technology (MIT) and National Centre for Nuclear Research (NCBJ) based program[23]

Its modus operandi is based on the fact that when a primary cosmic ray impacts with a nucleus in the upper atmosphere, the energies can be sufficiently large to break both the primary particle and the target nucleus through a nuclear interaction. Much of the energy of the collision goes to produce short-lived particles known as mesons, of which pions (π^+, π^-, π^0) and kaons (K^+, K^-, K^0) can be distinguished. Charged mesons decay very quickly, producing a muon and a neutrino, while neutral mesons decay much faster than charged mesons, preferably in gamma rays. Unlike neutral mesons, charged mesons are able to travel far enough before decaying to interact with another molecule. This interaction in turn can be in the form of another nuclear interaction just like the original cosmic ray interaction. The interaction can then produce even more mesons, contributing to the particle shower induced by the primary interaction. Thus, the cosmic ray muons (µ±) originate from the decay of the charged mesons.[24]

When a charged particle passes through a scintillating material, part of its energy is absorbed and reemitted as photons.

The Muon Detector consists of a 50×50×10 mm^3 extruded slab of plastic scintillator instrumented with a silicon photomultiplier (SiPM) which is a light-sensing device: photons incident on it can induce a Geiger discharge in the microcells of the SiPM, when the microcells discharge, they produce a measurable current. A single photon can trigger a single microcell, while multiple photons can trigger multiple cells. The current produced is sent through a custom-designed printed circuit board (PCB), which amplifies and shapes the signal so that it is suitable for measurement by a microcontroller. The Arduino Nano measures the time stamp of the event and the peak value on the analogue-to-digital converter (ADC). The measured peak ADC value can then be converted back into a peak SiPM voltage, which is proportional to the number of photons incident on the SiPM. If the measured ADC value is greater than a software-defined threshold, the microcontroller records the event data. In this way the number and the time of arriving of the photons is measured. [23,24]

Considering dimensions and weight given in the datasheet, the sensor is at the edge of the requirements of the rover, however, it can be reduced considerably by first removing the containment case and, if necessary, shrinking the PCB.

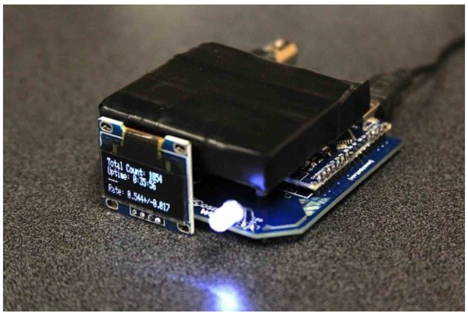

Figure 2.11: *CosmicWatch muon detector*

2.2.3 Lava tubes climate

The axial tilt of Mars' rotation axis causes seasons qualitatively similar to those on Earth, although the Martian surface experiences much greater temperature variations than those on Earth's surface.[25,26]

This is mainly because of the low density of the Martian atmosphere which contributes much less to the soil heat budget resulting in diurnal and seasonal variation of surface temperature larger than on Earth, since the Martian surface temperature is therefore essentially derived from a balance between the radiative terms and the conduction of soil heat. [27]

A further lack of moderation to these gradients is due to the absence of significant amounts of water, which on Earth acts as a damper through evaporation and condensation.[27]

Thermal inertia ($Jm^{-2}K^{-1}s^{-1/2}$) also influences daily temperature variations on the surface of Mars. This provides a measure of the ability to store heat during the day and re-radiate it at night and depends on factors such as particle size, rock abundance, degree of hardening and exposure of bedrock in the upper few centimetres of the subsurface. The temperature of a material with low thermal inertia varies significantly during the day, whereas the change is not as important in the case of higher values. In fact, Mars is found to have a lower thermal inertia than Earth from results derived from the thermal inertia mapping results derived from MGS - Thermal Emission Spectrometer (TES) [28]

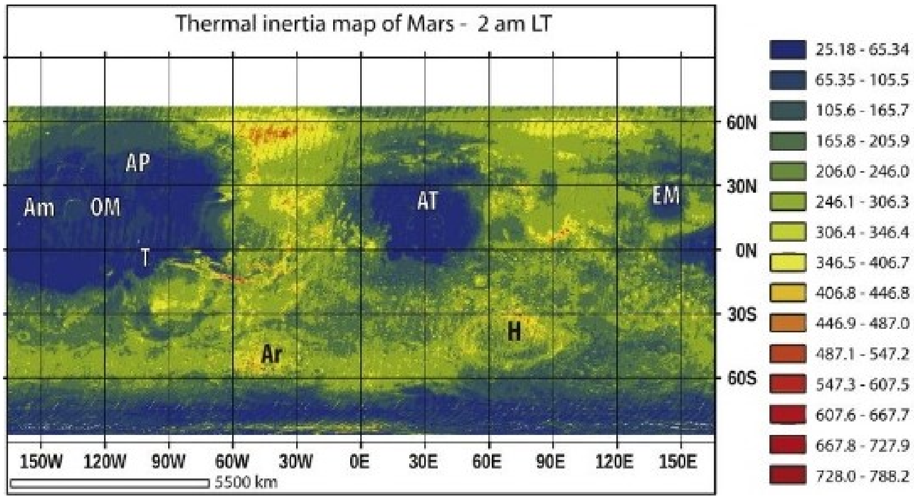

Figure 2.12: *Thermal Inertia data at night measured by TES*

In addition to MGS there have been different in situ missions such as Viking Landers 1 and 2, Mars Pathfinder, Phoenix and the Rover Environmental Monitoring Station (REMS) of the MSL that have assessed the Martian temperature leading to an average value of approximately 210K (against 287 K of average Earth temperature). In more detail, surface temperatures may reach a high of about 293 K at noon, at the equator, and a low of about 120 K at the poles. Actual temperature measurements at the Viking landers' site range from 256 K to 166 K. The warmest soil temperature estimated by the Viking Orbiter was 300 K. The Spirit rover recorded a maximum daytime air temperature in the shade of 308 K, and regularly recorded temperatures well above 273 K, except in winter.[25,27–29]

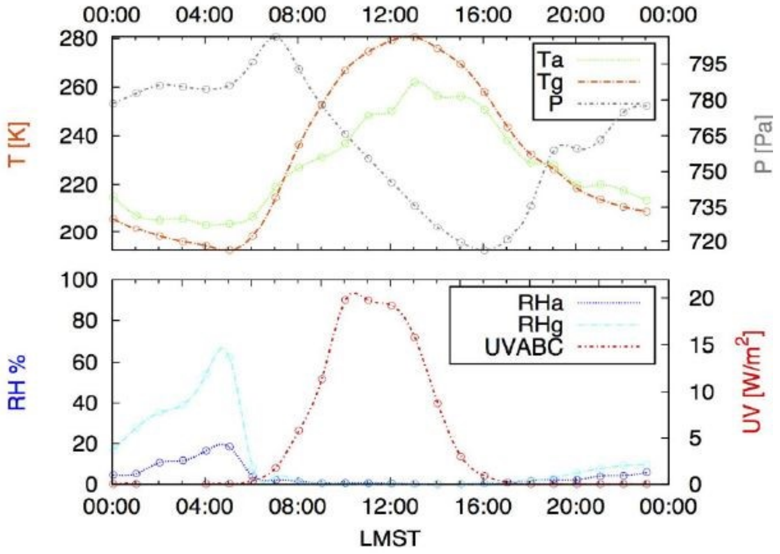

Figure 2.13: *REMS data of a typical Martian day*

REMS collected with the regularity and continuity atmospheric data at 1.7 m above the ground at different locations, in *fig. 2.13* are reported conditions recorded by REMS during a typical Martian day where T_a is the air temperature, T_g is the ground temperature, P is the atmospheric pressure. RH_a is the relative humidity measured in the air at the instrument, RH_g is the relative humidity in the interface layer close to the ground, and UV_{ABC} is the UV radiation.[30]

The reason why it is interesting to study temperature gradients inside pyroducts is that caves are often described as having a constant temperature because rock is slower to transmit heat and as the difference between summer and winter temperatures at the surface reach a cave, they balance each other out, so the average surface temperature becomes the ground temperature.

This isn't to say that there aren't temperature gradients inside, there can be large to small variations in temperature, in general the deeper you go into a cave, the smaller the changes. Therefore, it would be reasonable to expect lava tubes to show less variation.[31]

The study of the climatic environment of lava tubes does not stop at temperature alone; it is equally interesting to be able to describe the relative humidity conditions inside them because, as has already been said, since perchlorate could be present in the ground, these could attract water vapour and form hydrated salts or brines thanks to their hygroscopic properties.[30]

Aosong Electronics' DHT11 digital temperature and humidity sensor has been identified as the sensor to be mounted on board the rover. It is a calibrated digital output signal of the combined temperature and humidity sensor.

Its compact dimensions of 15.5 x 12 x 5.5 mm^3 meet the geometric requirements and it is possible to operate it in extreme conditions such as Martian temperatures.

Figure 2.14: *Aosong temperature and humidity sensor*

Chapter 3

Rover s modelling

Here the simulation of the robot and the method used are illustrated with focus on the implementation of the walking of the hexapod as well as on the servos chosen after the requirements were verified.

3.1. Walking theory

To get a hexapod to move in any direction the legs have to push it in that direction, with the result that the legs first move away from the body of the hexapod by lifting and then are brought back to the vicinity of the body through a cyclic movement consisting of two states: a *swing* phase and a *stance* phase.
In the swing movement, the insect's leg is lifted off the ground and brought from the PEP point (extreme posterior position) to a position where the next stance movement takes place, the AEP point (extreme anterior position), as illustrated in *fig.3.1* In the stance movement the legs have ground contact and the insect's body is supported by them and moved in the forward direction. The two phases of the leg movement are mutually exclusive; the legs cannot be in both phases at the same time. [1,32]
In the swing phase the leg moves parallel to the x-z plane therefore with y always constant.
The trajectories that can be imposed on the legs are numerous, in this work has been chosen to implement a circular movement when creating lift trajectory because in this way it's easier to avoid potential object as the leg will be high enough before any further walking movement. [32]
A semi-circular trajectory was set as the first test, but the simulation showed that in the gaits in which several legs were raised at the same time, lifting the legs the same amount of the advance caused oscillations of the main body, making it unstable. The semi-ellipse was chosen as it eliminated these oscillations by raising the leg less with the same amount of advance. By having the trajectory dependent from two semi-axes r_x and r_z, in the case of obstacles encountered on the path, it

is possible to manage the lift and advance independently by considering the equation:

$$\left(\frac{x}{r_x}\right)^2 + \left(\frac{z}{r_z}\right)^2 = 1 \qquad (1)$$

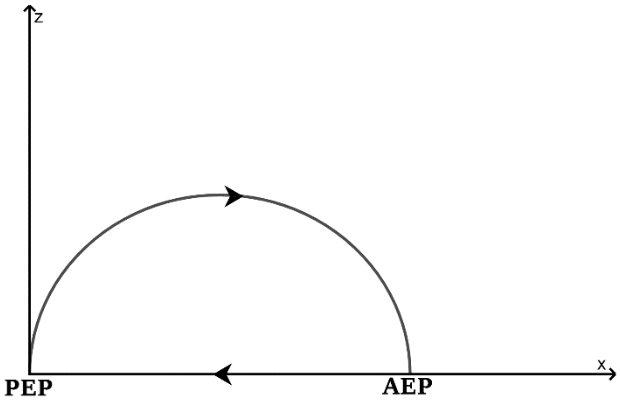

Figure 3.1: *Trajectory of each leg*

The stride of each leg, and therefore r_x, must be set considering the interference the legs would have with each other. The central leg on either side is the one which has less freedom of movement. In order to maintain the symmetry of the problem, equal steps were set for all the legs considering the constraints imposed by the central leg, *fig. 3.2,* whose limiting stride is 20 mm i.e. the anterior and posterior distance from the other two legs, which correspond to the value of 10 mm for the major semi-axis r_x.

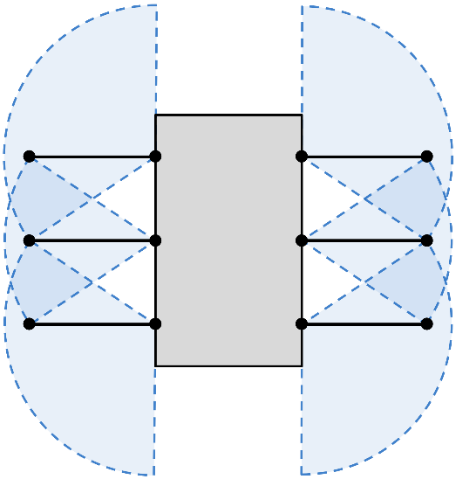

Figure 3.2: *Leg constraints*

In the stance phase, instead, the end of the legs through contact with the ground makes the robot to advance while the joints return in their original position with the movement from AEP to PEP in *fig.3.1.* If there was no friction the legs would go backwards without the robot advancing, the friction causes the end part to remain fixed not allowing the slipping.

To be able to implement the trajectory to each leg, it is necessary to know the angular position of every joint for every position imposed, this is calculated depending on the mechanical structure and on the dimensions of the robot. This type of gait control is called inverse kinematic control.

To this end the forward and the inverse kinematics of the system were studied to calculate the angular positions over time of the joints for both phases.

Forward kinematics determines the position and orientation of the End-Effector EE (which is the terminal part of the kinematic chain) when the joint configurations are known. These coordinates can be calculated using the transformation matrix which describes the transformation between frames starting from the Denavit-Hartenberg parameters (2).[33]

Table 3 shows these parameters that follows the convention for the case of the leg of the hexapod, where the SdR (system of reference) of the base is the one between the case and the Coxa (yellow in *fig.3.5*) and the SdR of the EE is at the end of the Tibia (green). In the table *ai* is the distance from z_i to z_{i+1} measured along x_i, a_i denotes the angle from z_i to z_{i+1} measured about x_i, d_i is the distance from x_{i-1} to x_i measured along z_i, and φ_i is the angle from x_{i-1} to x_i measured about z_i. where z_i is the rotation axis of the joint, x_i is along the direction orthogonal to z_i and z_{i-1}, positive from i to i+1 and y_i complete the triad.[33]

$c\varphi_1$ indicates the $cos\varphi_1$ and $s\varphi_1$ indicate the $sin\varphi_1$ for ease of writing and d_1 is the offset Femur d_2 offset Coxa as it can be seen in *fig.3.3*

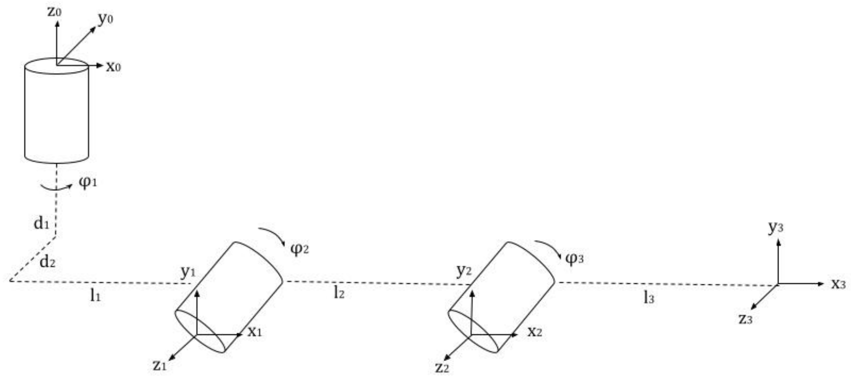

Figure 3.3: Kinematic chain of one leg

	a	a	d	$\boldsymbol{\varphi}$
1	$\sqrt[2]{l_1^2 + d_2^2}$	$\frac{\pi}{2}$	d_1	φ_1
2	l_2	0	0	φ_2
3	l_3	0	0	φ_3

Table 4: Denavit-Hartenberg parameters

$$
{}^{0}_{3}T = \begin{bmatrix} c\varphi_1 c\varphi_2 c\varphi_3 - c\varphi_1 s\varphi_2 s\varphi_3 & -c\varphi_1 c\varphi_2 s\varphi_3 - c\varphi_1 s\varphi_2 c\varphi_3 & s\varphi_1 & \sqrt[2]{l_1^2 + d_2^2}\, c\varphi_1 + l_2 c\varphi_1 c\varphi_2 + l_3(c\varphi_1 c\varphi_2 c\varphi_3 - c\varphi_1 s\varphi_2 s\varphi_3) \\ s\varphi_1 c\varphi_2 c\varphi_3 - s\varphi_1 s\varphi_2 s\varphi_3 & -s\varphi_1 c\varphi_2 s\varphi_3 - s\varphi_1 s\varphi_2 c\varphi_3 & -s\varphi_1 & \sqrt[2]{l_1^2 + d_2^2}\, s\varphi_1 + l_2 s\varphi_1 c\varphi_2 + l_3(s\varphi_1 c\varphi_2 c\varphi_3 - s\varphi_1 s\varphi_2 s\varphi_3) \\ c\varphi_2 s\varphi_3 + s\varphi_2 c\varphi_3 & c\varphi_2 c\varphi_3 - s\varphi_2 s\varphi_3 & 0 & d_1 + l_2 s\varphi_2 + l_3(c\varphi_2 s\varphi_3 + s\varphi_2 c\varphi_3) \\ 0 & 0 & 0 & 1 \end{bmatrix} \tag{2}
$$

As mentioned in the previous chapter when the transformation matrix from the base SdR to the EE SdR is known it is possible to switch to the reptilian configuration by imposing φ_2 equal to 0 ad φ_3 equal to $\frac{\pi}{2}$, as referred to the angles shown in *fig.3.4*, to calculate the initial positions of the end of the legs and then applying the trajectory.

On the other hand, inverse kinematics is determined to find the configurations to be assumed by the three joints to ensure that the position and orientation of the foot is as desired, as the leg can be described by its links and rotational joints.[33] These relations are usually highly non-linear and analytical or numerical solutions can only be obtained in special cases through the analysis of the robot's leg diagram and by setting two basic conditions: the kinematic chain is in the right workspace and the target point is reachable. [33]

Inverse kinematics has been calculated with the geometric method referred to the construction in *fig.3.4* [1] with a translation along x axis to take into account the d_2 segment of the Coxa which can be seen in *fig.3.5*

The calculations used the function **$atan2$** that considers the signs of the numerator and denominator as defined by (3).

$$atan2\left(\frac{y}{x}\right) = \begin{cases} atan\left(\frac{y}{x}\right) & x > 0 \\ atan\left(\frac{y}{x}\right) + \pi & y \geq 0, x < 0 \\ atan\left(\frac{y}{x}\right) - \pi & y < 0, x < 0 \\ \frac{\pi}{2} & y > 0, x = 0 \\ -\frac{\pi}{2} & y < 0, x = 0 \\ undefined & y = 0, x = 0 \end{cases} \tag{3}$$

In the following counts l_1, l_2 and l_3 are the length of the Coxa, Femur and Tibia respectively and assume the values in *Table 2*, d_1 6.27 mm is and d_2 id 7.25 mm

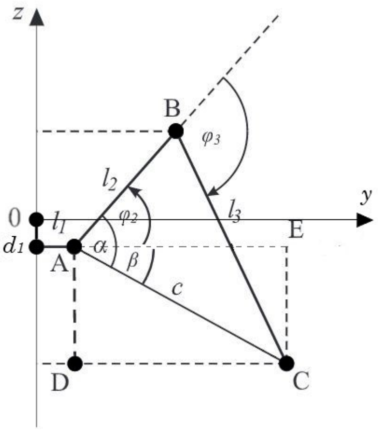

Figure 3.4: Geometric construction used for inverse kinematics

$$\varphi_1 = atan2\left(\frac{y}{x - d_2}\right) \tag{4}$$

$$\varphi_3 = acos\left(\frac{c^2 - l_2^2 - l_3^2}{2l_2l_3}\right) \tag{5}$$

$$c = (z - d_1)^2 + \left[\sqrt{(x - d_2)^2 + y^2} - l_1^2\right]^2 \tag{6}$$

$$\alpha = \cos^{-1}\left(\frac{l_3^2 - l_2^2 - c^2}{-2cl_2}\right) \tag{7}$$

$$\beta = atan2\left[\frac{z - d_1}{\sqrt{(x - d_2)^2 + y^2} - l_1^2}\right] \tag{8}$$

$$\varphi_2 = \alpha + \beta \tag{9}$$

After the calculation of the inverse kinematic the initial leg position was set arbitrarily with the aim of holding the robot's central body at a certain height above the ground, and at the same time testing with various simulations which configuration would result in the lowest torque applied to the joints.

Finally with reference to the SdR of *fig.3.5* the initial coordinates of the leg were defined, keeping the main body 15 mm above the ground but it is possible to lift it by only changing z_0; x_0, y_0 and z_0 (in *Table 4)* are the coordinates of the final part of the tibia in contact with the terrain and x_0 correspond to d_2 so that the leg is perpendicular to the edge of the case at the beginning of the step.

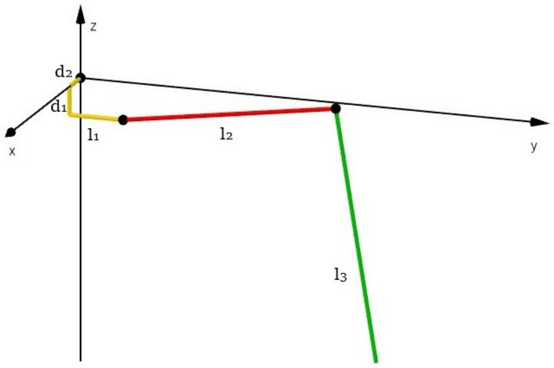

Figure 3.5: *Model in proportion of the leg. The yellow piece is the Coxa, the red one the Femur and the green one the Tibia. These colours have also been kept in Simulink.*

x_0	7.25 mm
y_0	50 mm
z_0	-45 mm

Table 5: Initial coordinates given to each leg

After defining the joints behaviour to obtain a specific type of trajectory, it remains to decide in what order the six legs should move to make the robot advance it in the desired direction. The gait, which is a defined sequence of leg movements coordinated, is periodic when the same states of the same leg during successive strokes occur at the same interval for all legs.

Some of the most common gaits are the metachronal gait, the ripple gait and the tripod gait, which are used for slow, medium and fast movements, respectively. The fundamental difference between these gaits is the use of one, two or three legs at the same time during the swing phase.

Fig.3.6 shows the diagram of these gaits where the white colour indicates that the foot is in contact with the ground and the black colour the opposite.

The metachronal gait (a) is the one that assures the greatest stability, it is a gait that the hexapod adopts when moving slowly, as only one leg is lifted at a time, with the other five lowered, so that the hexapod is always in a highly stable posture due to the greater number of legs on the ground. All legs on one side are moved forward in succession in a gait that propagates from back to front. Each leg has a separate cycle, having six different cycles until the hexapod returns to its initial state.

The Ripple gait (b) is very similar to the metachronal gait but allows for a faster movement. Propagation from back to front occurs simultaneously on each side with one side in delay. The diagonal legs swing at the same time, and the middle legs swing during a pause for the other side. This results in four cycles and a minimum of four legs always touching the ground.

The tripod gait (c) allows the fastest movement and contains only two cycles. The front and rear legs of the same side and the middle leg of the opposite side combined move in altered cycles. One tripod swing while the other maintains the balance of the robot.

These processes are repeated to achieve a straight-line walk. The advantage of this method is that at least three alternating legs always remain on the ground, always creating a triangle projected onto the ground. This triangle always encloses the geometric centre of gravity of the body, ensuring stability.[2,32,34]

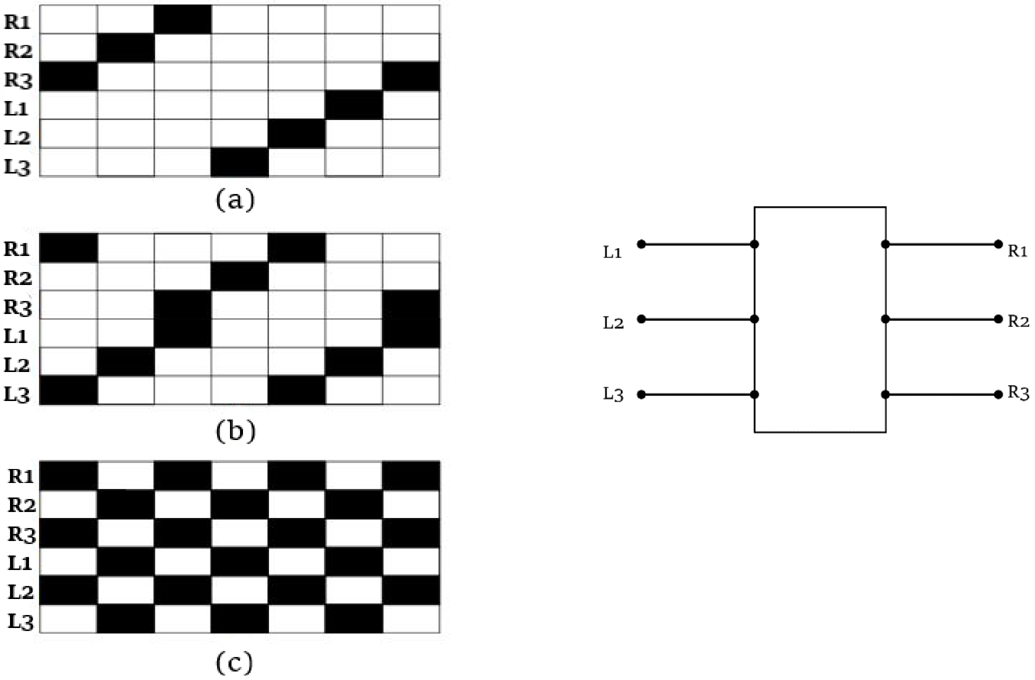

Figure 3.6: *Gait diagram: a) Metachronal gait; b) Ripple gait; c) Tripod gate*

There are a few methods that can be used for hexapods to rotate. The basic method is to change the stride length on one side. By decreasing or increasing the stride length, one side will move slower or faster respectively, making the rotation possible.

It is possible to achieve very tight turns, even turning in place, by stepping legs backwards. For example, for the left turn, considering the tripod gait (but the same reasoning can be applied to all gaits), legs L1 and L3 move backwards by -r_x and leg R2 moves forward by r_x. Then, in the second phase, legs R1 and R3 move forward by r_x, while leg L2 moves backwards by -r_x. Therefore, the hexapod will rotate 45° to the left. For rotation to the right, it will be sufficient to move the right leg by -r_x and the left leg by r_x in the same way.[32,35]

3.2. Simulation

MATLAB&Simulink environment was used to simulate the robot's dynamics and whether the actuators identified were suitable to implement the various gaits discussed in the previous chapter.

Simulink is a MATLAB-based environment that makes it possible to model and simulate dynamic systems. Its main interface consists of a graphical block diagram tool and a customizable set of block libraries. It offers integration with the rest of the MATLAB environment thus allowing the needed scripts for the various robot gaits to be created directly in MATLAB and then called in Simulink.[36]

Has been used *Simscape multibody*, which is a software developed by MathWorks to model mechanical systems, in which the model is constructed using solid bodies, connected to coordinate frames. These coordinate frames are then connected by rigid transformations or joints. Joints allow several DoF between two frames, up to a maximum of six, while rigid transformations do not allow any DoF. The revolute joints that are used in this model allow only one DoF and can be driven using either a torque or a motion input, in the second one are required position, velocity, and acceleration as a function of time. A range of values such as position, velocity, acceleration, and torque can also be sensed via the block.[32]

Physical properties can be assigned to each solid body manually or by importing them. Through *Simscape Multibody link* it is possible to export CAD models and to import them into *Simscape*, during this export a *DataFile.m* is created in MATLAB that contains all the information related to the CAD model such as rigid transformations between elements, masses, centres of mass, and other inertia data for each element.[32]

In *fig. 3.7* is shown the model of the leg imported from Solidworks where can be identified the rigid rotations, solid bodies and revolute joints that correspond to the servos.

Fig. 3.8, on the other hand, is a model of the entire system, complete with gait commands and ground contact.

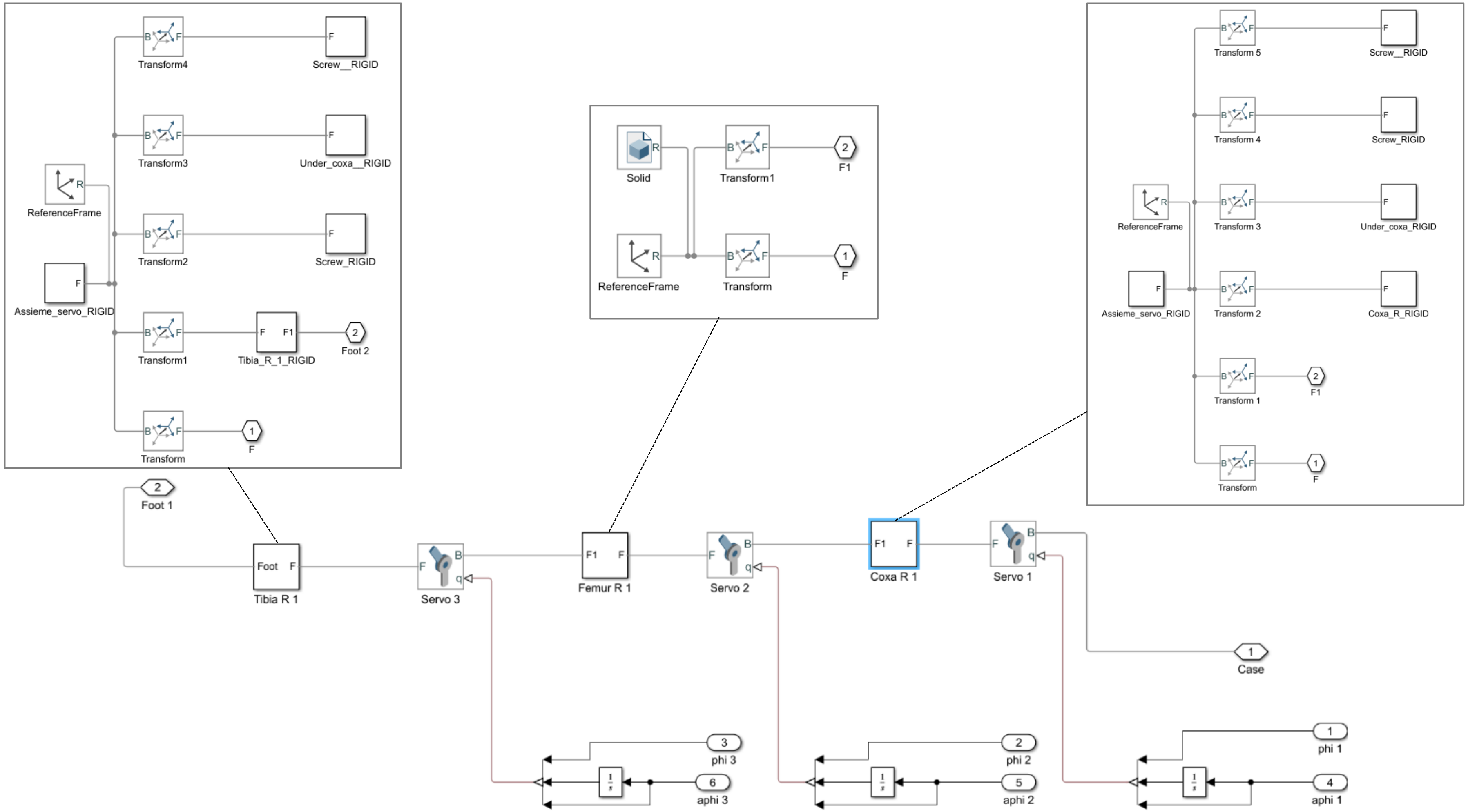

Figure 3.7: Simulink modelling of one leg

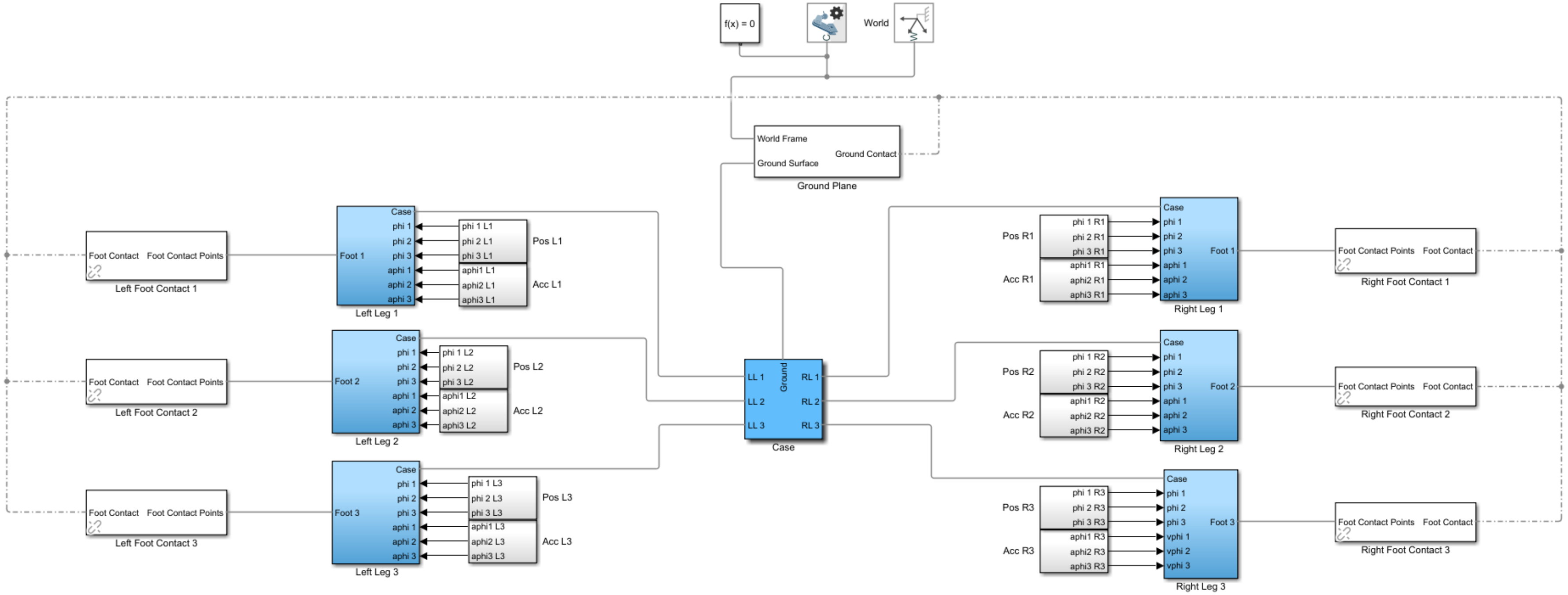

Figure 3.8: *Simulink modelling of the entire system*

To make the robot advance after each cycle instead of staying in place by slipping, it is necessary to model the contact with the ground. This has been done in Simulink using the *Spatial contact forces* block that models the contact between geometries associated with a pair of bodies.

During contact, each geometry has a contact frame. The two contact frames are always coincident and coincide with the contact point.

The block applies the contact forces to the geometries at the origin of the contact frame in accordance with Newton's Third Law: the normal force is aligned with the z-axis of the contact frame which is directed along the outgoing normal to the base, it prevents penetration; the friction force, which is in the contact plane, opposes the relative tangential velocities between the geometries.[37]

For each foot, four spheres of radius 0.5 mm were defined, positioned at the vertices of the rectangle representing the footprint of each leg with the dimensions of 4.5x1.5 mm^2.

The *Spatial Contact Force* block was applied to each of these spheres, defining the contact with a plane that was created to form the ground on which the hexapod walks.

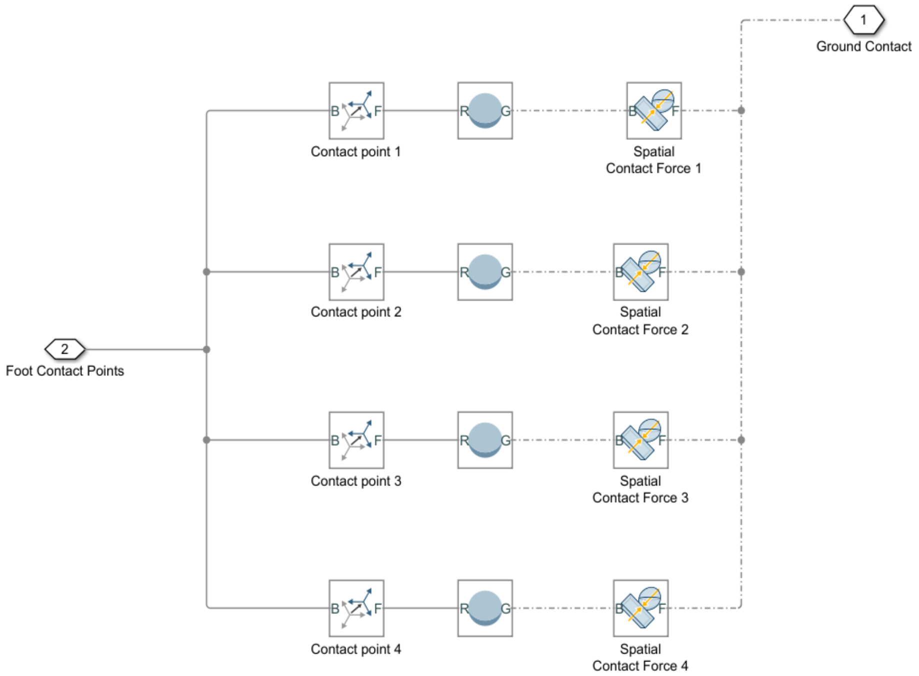

Figure 3.9: *Simulink modelling of the contact with the ground*

Finally, was used the *6-DOF joint* block between the main reference system of the robots and that of the ground, which represents a joint with three prismatic type couplings and the three revolute type couplings between the two reference systems.

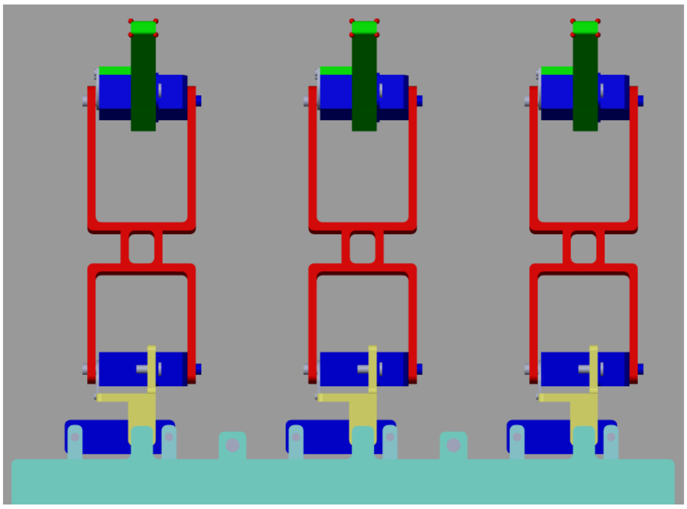

Figure 3.10: *Zoom of the contact points on Simscape Multibody*

To make each leg of the rover follow a semi-ellipse, was applied the inverse kinematics control method defined above via a specially created function *invkinematics.m.* After finding the position of the joints such that the main body of the rover was supported and which resulted in lower torques applied to the joints, were defined the parameters for the trajectory and they were applied to the foot of each leg. The greatest possible advance relative to the constrains was chosen, resulting in giving the ellipse a major semi-axis r_x equals to 9 mm, while, to avoid oscillations of the main body when the number of legs supporting it is low, a minor semi-axis r_z of 5 mm was placed. The semi-ellipse is traveled by each leg of the rover in a time $t_{movement}$ of 4 s.

The angles of the joints in the PEP position, φ_1, and in the AEP, φ_{end} , can be seen in *Table 5* with reference to the angles in *fig. 3.4.*

	PEP	AEP
$\boldsymbol{\varphi_1}$	0	-0.3455 rad (-19.7989°)
$\boldsymbol{\varphi_2}$	0.1289 rad (7.3897°)	0.1395 rad (7.9969°)
$\boldsymbol{\varphi_3}$	-1.4418 rad (82.6103°)	-1.4312 rad (82.0031°)

Table 6: Joint angles at the start and at the end of the semi-ellipse. (Positive values means counter clockwise)

After deciding on the trajectory, position, velocity and acceleration can be defined. These are dependent on parameters that determine the number of points on the trajectory. The parameters are the step length (`2*rx`), the step height (`rz`), the step time (`tmovement`) and the sample (`step`).

These are defined in an initial *init.m* script along with the geometry, in *init.m* there is also the possibility to choose the type of gait to impose to the robot via the *velocity* variable which can assume the value of 1 making the robot do metachronal gait, 2 for ripple gait and 3 for tripod by calling the scripts for each gait analysed.

These scripts create a vector of two columns where instants of time, sampled at a step size of $1.501*10^{-3}$ s, are recorded in the first column and angle profiles are recorded in the second one. The vector is generated for successive swing phases, by applying the semi-elliptical trajectory to the EE of the legs, according to the order in *fig.3.6,* for each gait, leaving constant the angles of the leg joints that in that fraction of the period are not implemented, the initial or final position in which they can be depends on whether they have already been implemented or not.

As the revolute joint needs as input the profiles of position, speed and acceleration, the derivation of the the joint profile over time would yield the velocity profile to be applied to the revolute joint, and a second derivation over time would yield the acceleration profile.

However, in the swing phase, doing so resulted in a discontinuous velocity profile that led in potentially damaging peaks and oscillations, it was therefore decided to set up trapezoidal velocity profiles where the positioning time was equivalent to 30% of $t_{movemet}$.

The Jerk (which is the derivative of the acceleration) still resulted in infinite values since the acceleration was still discontinuous, it was finally chosen to modify the trajectory planning, giving continuity to the acceleration profile, which takes trapezoidal evolution in the two phases of initial acceleration and final deceleration, thus having a connected velocity pattern.[33]

In the last fraction of the period of the gait the stance phase occurs and thus the rover's advance and the return of all joints to their initial position. This phase also evolves in a $t_{movement}$ of 4 s and it was chosen to impose a progression with a fifth-degree polynomial on the joints[33]:

$$\varphi(t) = a_0 + a_1 t + a_2 t^2 + a_3 t^3 + a_4 t^4 + a_5 t^5 \tag{10.1}$$

$$\dot{\varphi}(t) = a_1 + 2a_2 t + 3a_3 t^2 + 4a_4 t^3 + 5a_5 t^4$$

(10.2)

$$\ddot{\varphi}(t) = 2a_2 + 6a_3t + 12a_4t^2 + 20a_5t^2$$

(10.3)

The values of the a_i are obtained by setting the initial and final values of position, velocity and acceleration:

$$\varphi(0) = \varphi_0$$

$$\varphi(t_{movement}) = \varphi_{end}$$

$$\dot{\varphi}(0) = \dot{\varphi}(t_{movement}) = \ddot{\varphi}(0) = \ddot{\varphi}(t_{movement}) = 0$$

(11)

Resulting in:

$$\begin{cases} a_0 = \varphi_0 \\ a_1 = 0 \\ a_2 = 0 \\ a_3 = \dfrac{10(\varphi_{end} - \varphi_0)}{t^3} \\ a_4 = \dfrac{-15(\varphi_{end} - \varphi_0)}{t^4} \\ a_5 = \dfrac{6(\varphi_{end} - \varphi_0)}{t^6} \end{cases}$$

(12)

The resulting vectors are not all the same size for every gait, since the period of each depends on the number of legs implemented at the same time. The position and acceleration vectors of the Metachronal gait are 18655x2, those of the Ripple gait are 13325x2 and those of the Tripod gait are 7995x2.

After printing one position vector and one acceleration vector, both of the same length, for each joint of each leg, the vectors were called into the Simulink environment and was used the block *Repeating Sequence Stair* which was intended to make this vector become periodic throughout the simulation time, repeating it. These vectors then were connected to the revolute joint. The velocity vector was obtained by integrating, via the *Integrator* block, the acceleration by setting the velocity of each joint equal to 0 as an initial condition. The position, velocity and acceleration profiles imposed on the joints can be seen in *fig. 3.11* and *fig 3.12,* in this case they are the ones for leg L2 for the Tripod gait, but they turn out to have the same profiles for all legs for each gait, only change the time they are applied and the interval between swing and stance phases.

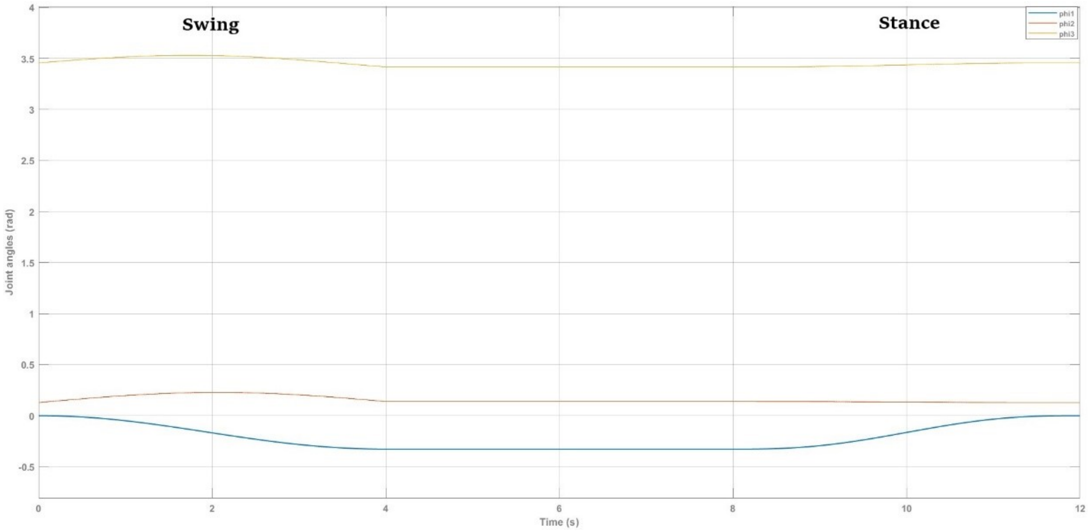

Figure 3.11: *Position profiles imposed to L2 for the Tripod gait*

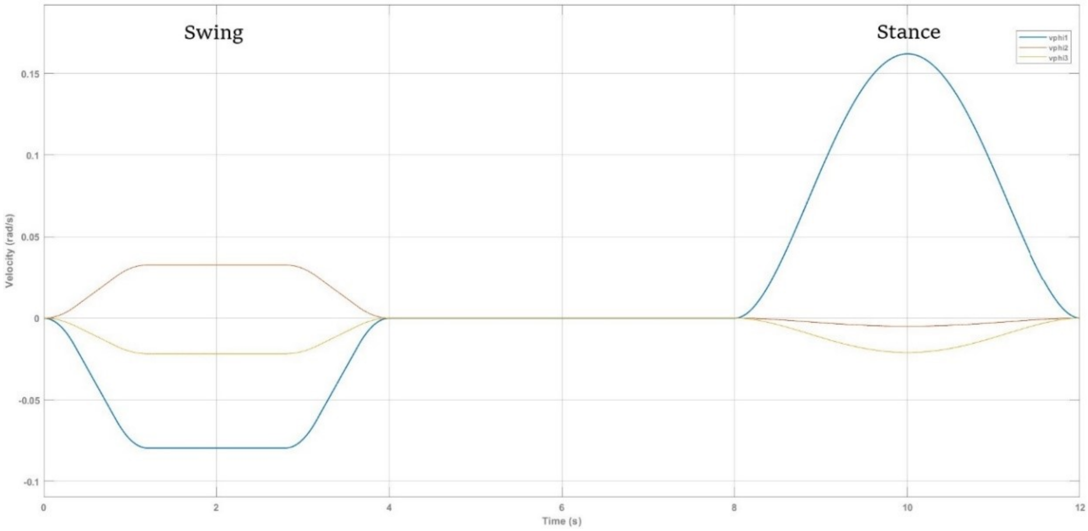

Figure 3.12: *Velocity profile imposed to L2 for the Tripod gait*

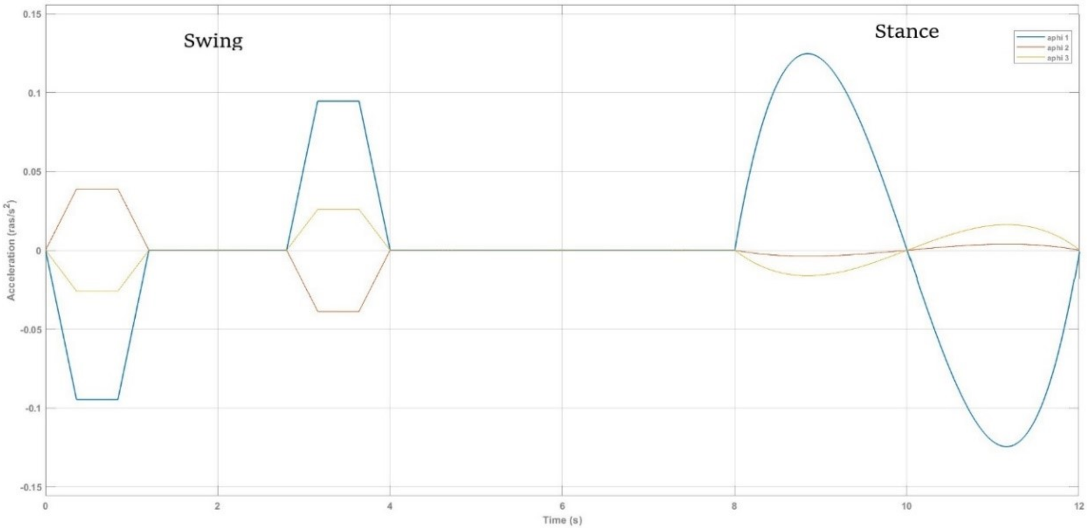

Figure 3.13: *Acceleration profile imposed to L2 for the Tripod gait*

This pages present some of the code used in MATLAB to generate the vectors needed for the movement.

Joint position generation for the first swing phase of the tripod gait:

```
for t=0:step:tmovement

    xnew = x0 + rx*(1- cos((pi*t)/tmovement));
    ynew = y0;
    znew = z0 + rz*sin((pi*t)/tmovement);

    [phi1_R1, phi2_R1, phi3_R1] =invkinematicsR(xnew, ynew ,znew);
    [phi1_L2, phi2_L2, phi3_L2] =invkinematicsL(xnew, ynew ,znew);
    [phi1_R3, phi2_R3, phi3_R3] =invkinematicsR(xnew, ynew ,znew);

    phi1R1(i,:)=[t phi1_R1];
    phi2R1(i,:)=[t phi2_R1];
    phi3R1(i,:)=[t phi3_R1];

    phi1L2(i,:)=[t phi1_L2];
    phi2L2(i,:)=[t phi2_L2];
    phi3L2(i,:)=[t phi3_L2];

    phi1R3(i,:)=[t phi1_R3];
    phi2R3(i,:)=[t phi2_R3];
    phi3R3(i,:)=[t phi3_R3];

    %Le altre gambe rimangono ferme nella loro posizione iniziale

    phi1R2(i,:)=[t phi1_R0];
    phi2R2(i,:)=[t phi2_R0];
    phi3R2(i,:)=[t phi3_R0];

    phi1L1(i,:)=[t phi1_L0];
    phi2L1(i,:)=[t phi2_L0];
    phi3L1(i,:)=[t phi3_L0];
    phi1L3(i,:)=[t phi1_L0];
    phi2L3(i,:)=[t phi2_L0];
    phi3L3(i,:)=[t phi3_L0];

    i=i+1;
end
```

Joint position generation for the stance phase of the tripod gait:

```
for t= 0:step:tmovement

      [phi1R_0,phi2R_0,phi3R_0]=invkinematicsR(xnewR1, y0 ,z0);
      [phi1L_0,phi2L_0,phi3L_0]=invkinematicsL(xnewL1, y0 ,z0);

      [phi1R_end,phi2R_end,phi3R_end]=invkinematicsR(x0, y0 ,z0);
      [phi1L_end,phi2L_end,phi3L_end]=invkinematicsL(x0, y0 ,z0);


      phi1_R= phi1R_0 + ((10*(phi1R_end-phi1R_0))/(tmovement)^3)*(t)^3+...
```

```
                        ((-15*(phi1R_end-phi1R_0))/(tmovement)^4)*(t)^4 +...
                        ((6*(phi1R_end-phi1R_0))/(tmovement)^5)*(t)^5;

        phi2_R= phi2R_0 + ((10*(phi2R_end-phi2R_0))/(tmovement)^3)*(t)^3 +...
                        ((-15*(phi2R_end-phi2R_0))/(tmovement)^4)*(t)^4 +...
                        ((6*(phi2R_end-phi2R_0))/(tmovement)^5)*(t)^5;

        phi3_R= phi3R_0 + ((10*(phi3R_end-phi3R_0))/(tmovement)^3)*(t)^3 +...
                        ((-15*(phi3R_end-phi3R_0))/(tmovement)^4)*(t)^4 +...
                        ((6*(phi3R_end-phi3R_0))/(tmovement)^5)*(t)^5;

        phi1_L= phi1L_0 + ((10*(phi1L_end-phi1L_0))/(tmovement)^3)*(t)^3 +...
                        ((-15*(phi1L_end-phi1L_0))/(tmovement)^4)*(t)^4+...
                        ((6*(phi1L_end-phi1L_0))/(tmovement)^5)*(t)^5;

        phi2_L= phi2L_0 + ((10*(phi2L_end-phi2L_0))/(tmovement)^3)*(t)^3 +...
                        ((-15*(phi2L_end-phi2L_0))/(tmovement)^4)*(t)^4 +...
                        ((6*(phi2L_end-phi2L_0))/(tmovement)^5)*(t)^5;

        phi3_L= phi3L_0 + ((10*(phi3L_end-phi3L_0))/(tmovement)^3)*(t)^3 +...
                        ((-15*(phi3L_end-phi3L_0))/(tmovement)^4)*(t)^4 +...
                        ((6*(phi3L_end-phi3L_0))/(tmovement)^5)*(t)^5;

        phi1R1(i,:)=[t phi1_R];
        phi2R1(i,:)=[t phi2_R];
        phi3R1(i,:)=[t phi3_R];

        phi1R2(i,:)=[t phi1_R];
        phi2R2(i,:)=[t phi2_R];
        phi3R2(i,:)=[t phi3_R];

        phi1R3(i,:)=[t phi1_R];
        phi2R3(i,:)=[t phi2_R];
        phi3R3(i,:)=[t phi3_R];

        phi1L1(i,:)=[t phi1_L];
        phi2L1(i,:)=[t phi2_L];
        phi3L1(i,:)=[t phi3_L];

        phi1L2(i,:)=[t phi1_L];
        phi2L2(i,:)=[t phi2_L];
        phi3L2(i,:)=[t phi3_L];

        phi1L3(i,:)=[t phi1_L];
        phi2L3(i,:)=[t phi2_L];
        phi3L3(i,:)=[t phi3_L];

        i=i+1;
end
```

In *fig. 3.13* there is the upper view of the model of the robot generated with *Simscape Multibody* while implementing the first and the second swing phases of the tripod gait.

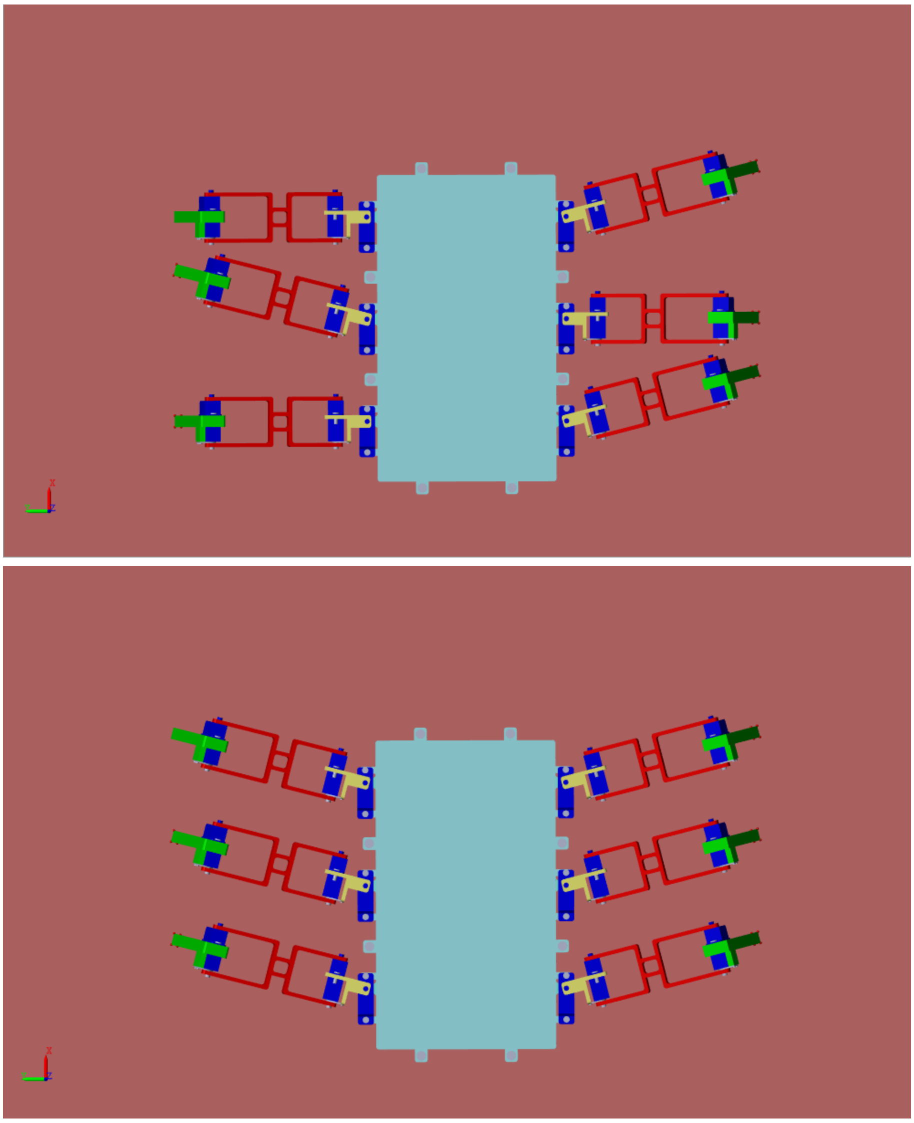

Figure 3.14: *Subsequent swing phase for Tripod gait modelled in Simscape Multibody*

3.3. Actuators

After using the methods described above to simulate the robot's gait, thanks to joint revolute, that is able to detect the applied torques, was studied the dynamics of the rover during the various phases of its gait. The purpose was to verify that the actuators were congruent with the needs of the design.

The torques explicated by the joints (Nm) were plotted as a function of time (s). The graphs are arranged in chronological order of implementation for the legs during the gait period; in the tripod gait, for brevity, have been shown the graphs relating only to the legs that are activated in the first period. In fact, the profiles of the torques of the other three are symmetrical.

In the graphs that will be presented, the blue colour indicates the torque explicated by the joint between the case and Coxa, the red colour the torque explicated by the joint between the Coxa and Femur, and the yellow colour the torque explicated by the joint between the Femur and Tibia.

As can be seen, the joint that requires the most torque during movement is the one connecting the Coxa and the Femur, which is mainly responsible for lifting the leg from the ground and unlike the third joint, the one between Femur and Tibia, has the weight of the Femur in addition to the weight of the Tibia.

The torque of the first joint, between the case and the Coxa, is very low compared to the other two, this is because it does not have to counteract the torque resulting from the force of gravity applied to the various pieces of the legs, which the other two joints have to face because they have their axis perpendicular to the direction of the force of gravity.

Using a $t_{movement}$ of 4 s and the correct starting configuration, each joint is within the servo's torque limits, in some cases reaching a maximum of 0.065Nm due to the peaks which, although they have been considerably reduced using trapezoidal acceleration profiles and a not-too-low $t_{movement}$, are still present but limited to values lower than the holding torque indicated in the datasheet of the servo.

After defining the optimal $t_{movement}$ with regard to the simulation results, the average speed can be calculated. The rover advances 9 mm every period, in the case of the metachronal gait the period is $7t_{movement}$, i.e. 28 s, so we obtain an average robot speed of 0.32 mm/s ($3.2*10^{-4}$ m/s), the ripple gait period on the other hand is $5t_{movement}$, i.e. 20 s, which corresponds to a speed of 0.45 mm/s ($4.5*10^{-4}$ m/s) and finally the tripod gait which is the fastest gait having a period of only $3t_{movement}$, i.e. 12 s, lets the robot have an average speed of 0.75 mm/s ($7.5*10^{-4}$ m/s).

The CAD modelling of the hexapod was based on the identified servo, using the servo drawing files found on the site, the model was recreated in Solidworks. It is the smallest servo found on the market and this is what made it possible to make the robot so miniaturised, considering the servo housings inside the leg parts. The servo is the *C017CLS* which is a digital servo that works with PWM control. The type of motor is a coreless DC motor, which makes it possible to reduce the overall weight of the servo to the quite low mass of 1.7 g.

The manufacturer's datasheet shows the stall torque it can produce, which is the torque produced when its rotational speed is zero; this is 0.075 Nm and has been taken as the maximum torque limit for the model, although the maximum torque measured in simulations and set as the limit is approximately 15% lower, for conservative reasons.

While the limits for torque may be quite strict for the model, those for speed are not. Since it is stated on the manufacturer's website that the servo is also suitable for miniaturised drones and helicopters, it can reach quite high speeds. In particular, operating speed, which is defined as the time required to reach a specific position, is 0.0700 sec/60°, which corresponds to 200 rpm (20.94 rad/s).

The choice of this servo was also supported by the fact that it is possible to obtain position feedbacks thanks to an angular sensor, which is useful in the future for modelling a feedback control via PID in order to eliminate peaks and oscillations seen in the graphs, as this is a preliminary simulation useful to decide which elements to include.

The dimensions of the servo (in mm) are shown in fig. 3.14 where there are the tables used for the CAD model.

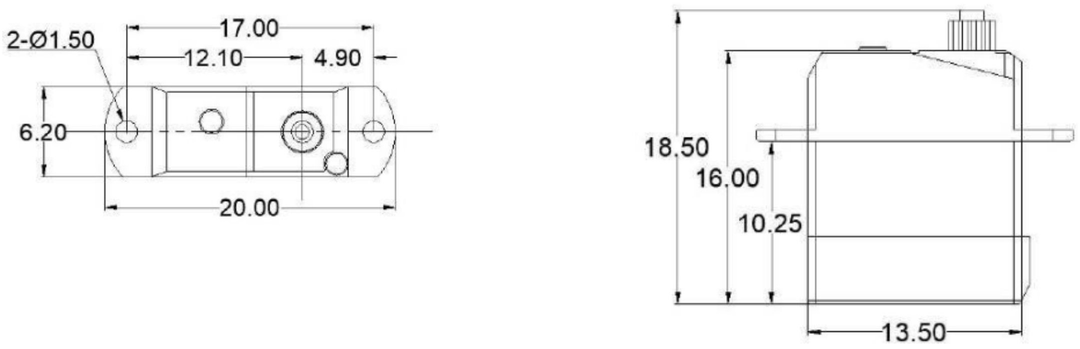

Figure 3.15: *Servo draw*

3.3.1 Metachronal gait

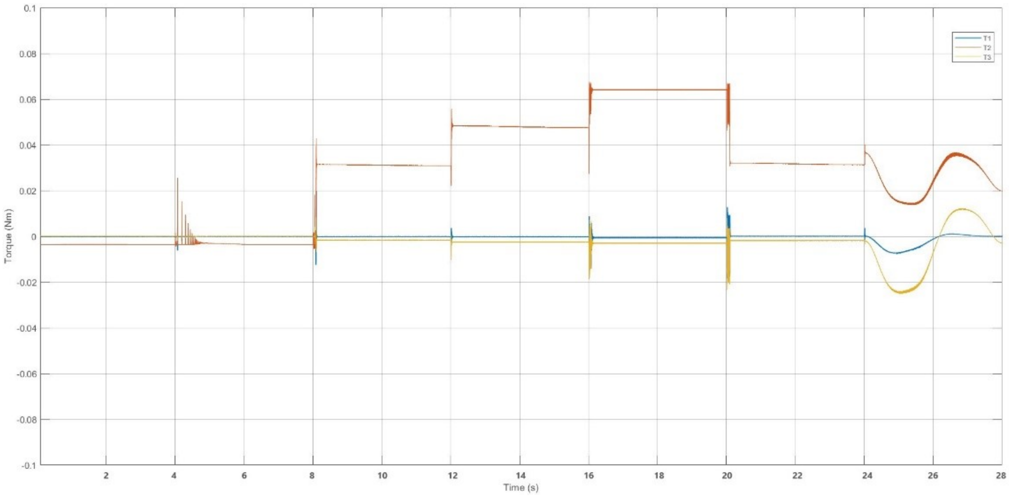

Figure 3.16: *R3 – Swing movement in the first fraction of metachronal period*

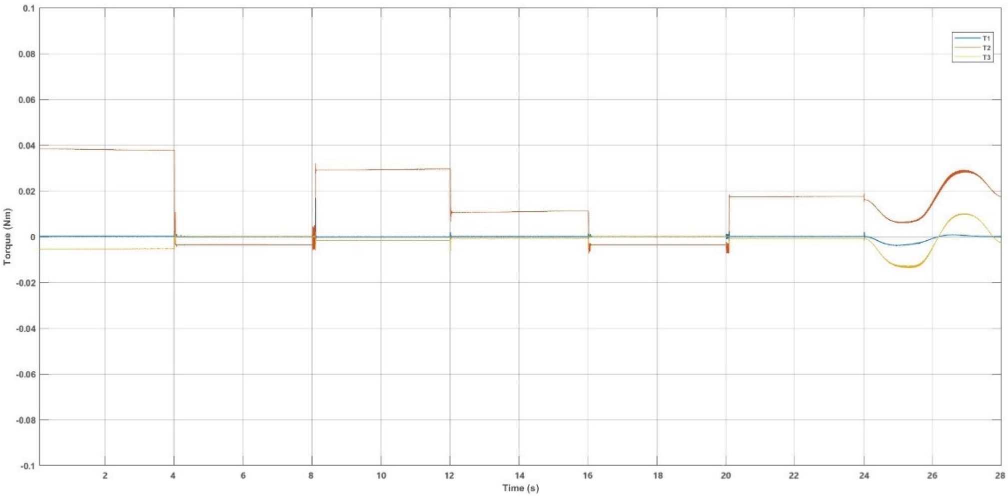

Figure 3.17: *R2 – Swing movement in the second fraction of metachronal period*

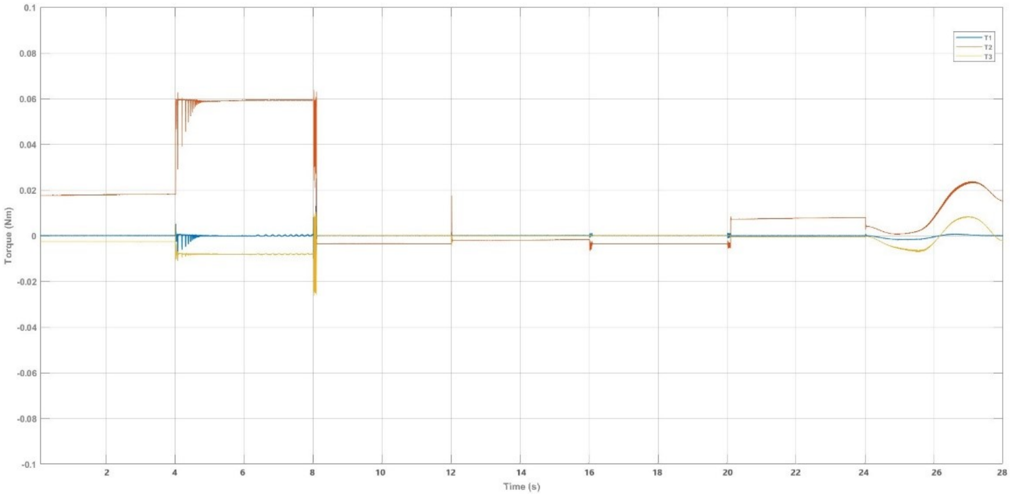

Figure 3.18: *R1 – Swing movement in the third fraction of metachronal period*

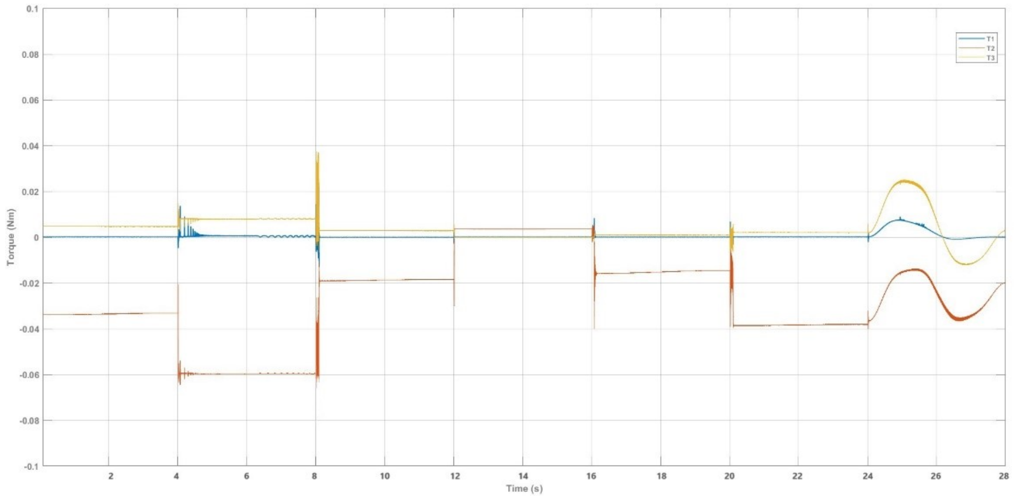

Figure 3.19: *L3 – Swing movement in the fourth fraction of metachronal period*

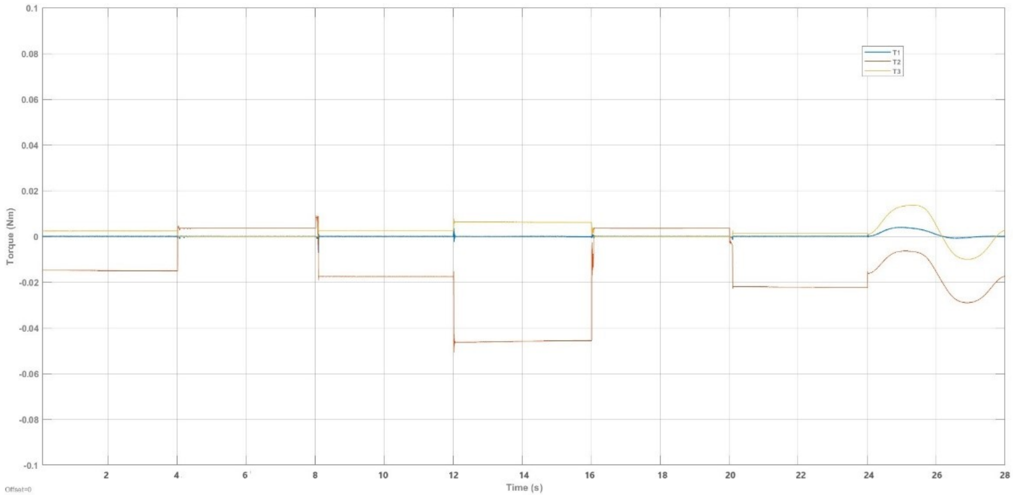

Figure 3.20: *L2 – Swing movement in the fifth fraction of metachronal period*

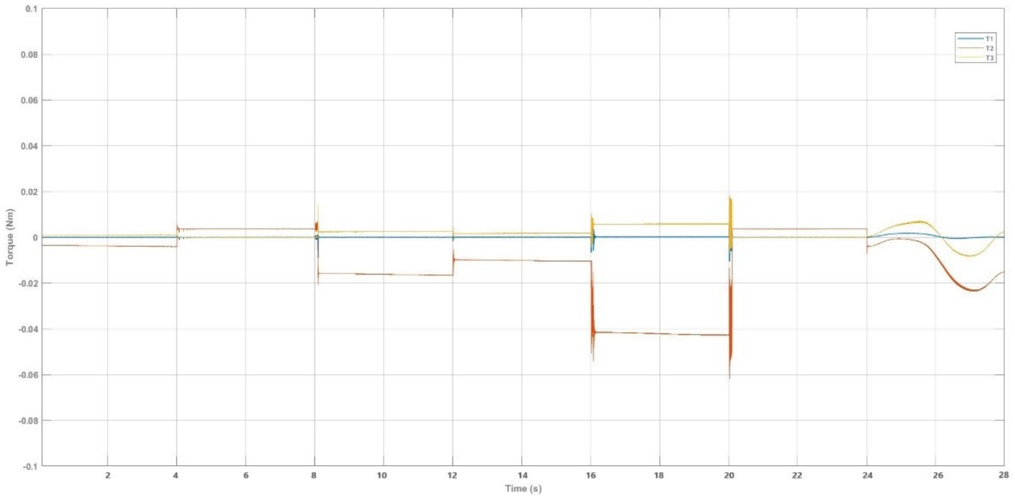

Figure 3.21: *L1 – Swing movement in the sixth fraction of metachronal period*

3.3.2 Ripple gait

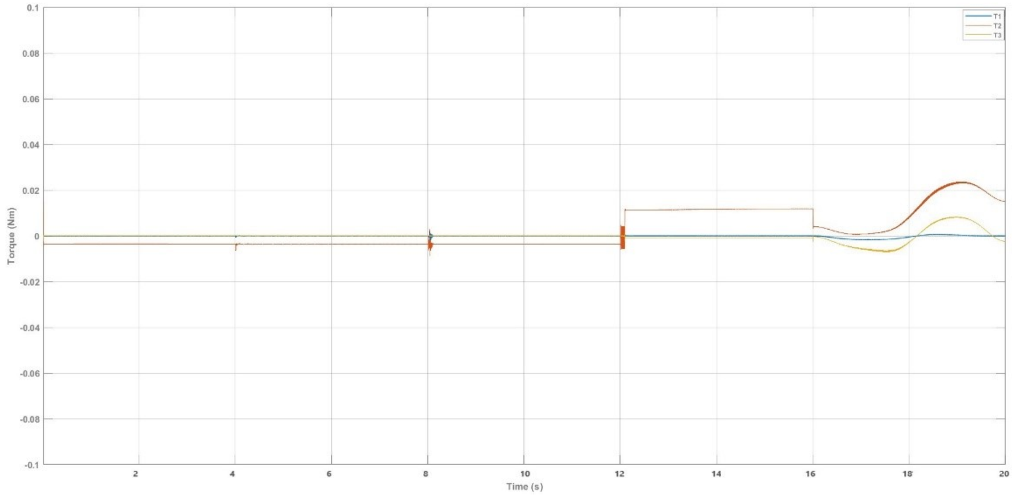

Figure 3.22: *R1 – Swing movement in the first fraction of ripple period*

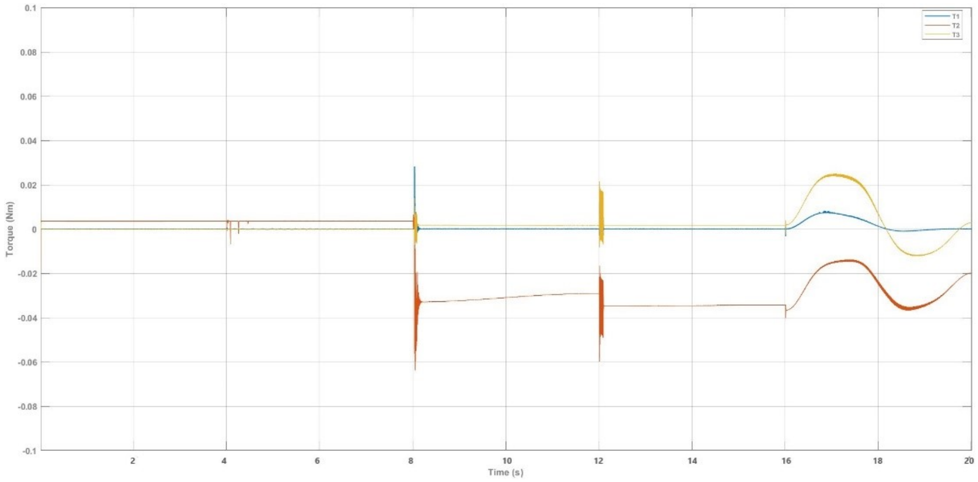

Figure 3.23: *L3 – Swing movement in the first fraction of ripple period*

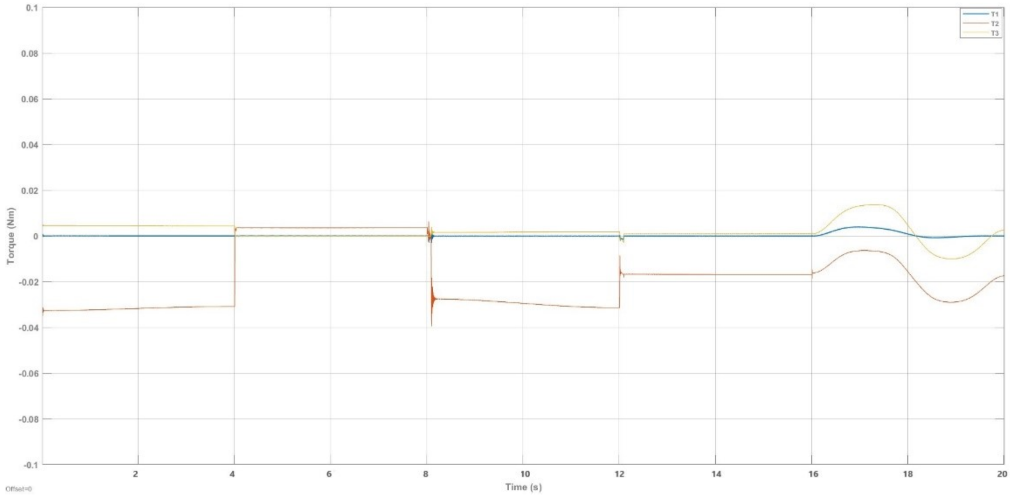

Figure 3.24: *L2 – Swing movement in the second fraction of ripple period*

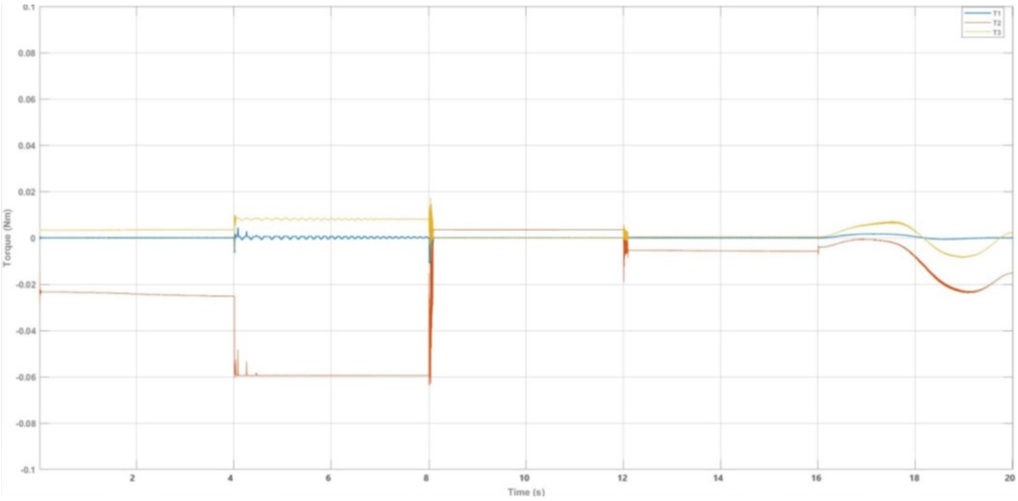

Figure 3.25: *L1 – Swing movement in the third fraction of ripple period*

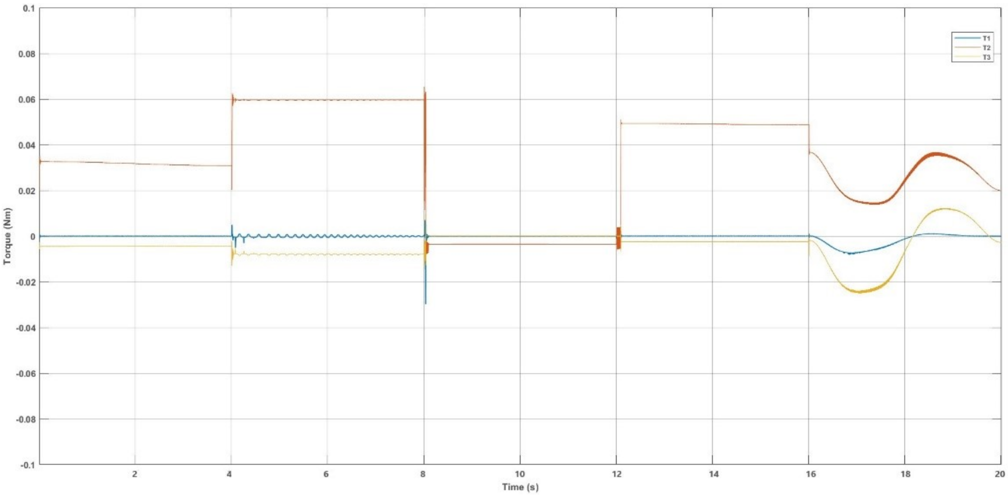

Figure 3.26: *R3 – Swing movement in the third fraction of ripple period*

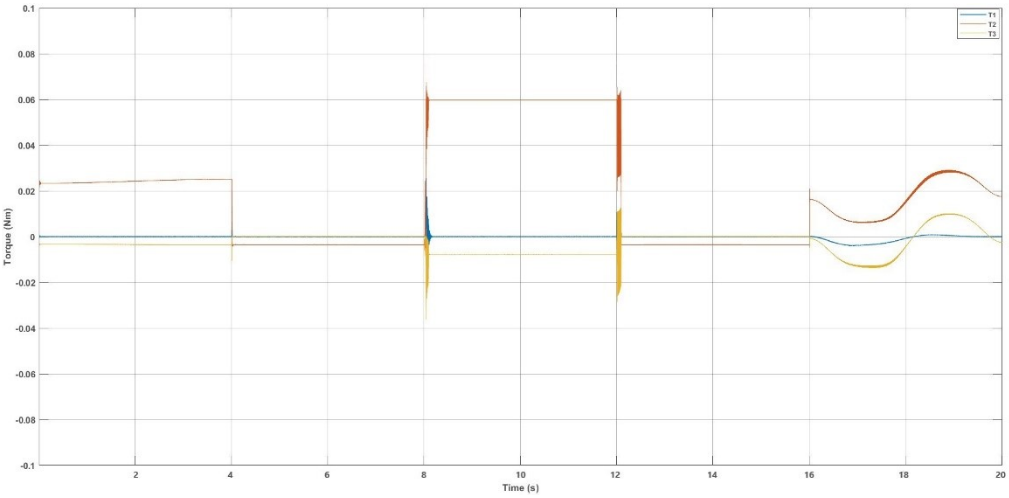

Figure 3.27: *R2 – Swing movement in the fourth fraction of ripple period*

3.3.3 Tripod gait

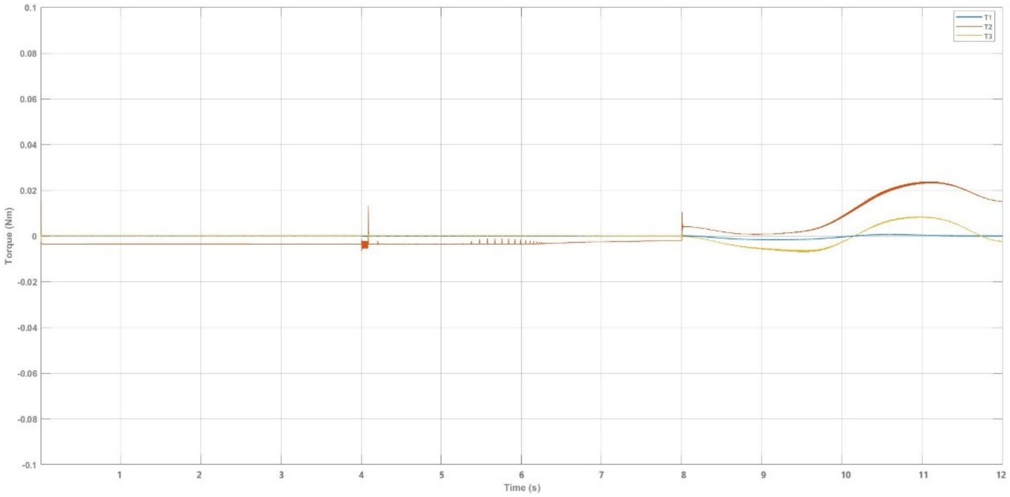

Figure 3.28: *R1 – Swing movement in the first fraction of tripod period*

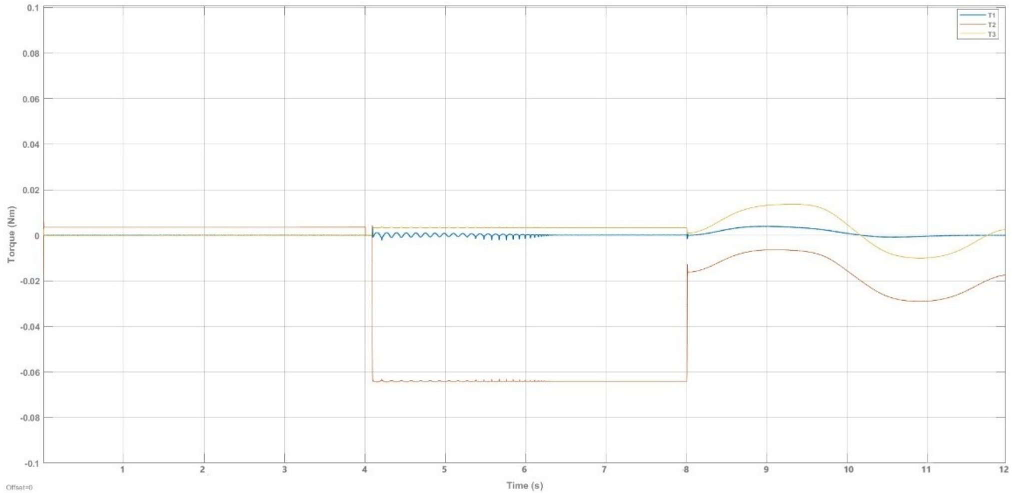

Figure 3.29: *L2 – Swing movement in the first fraction of tripod period*

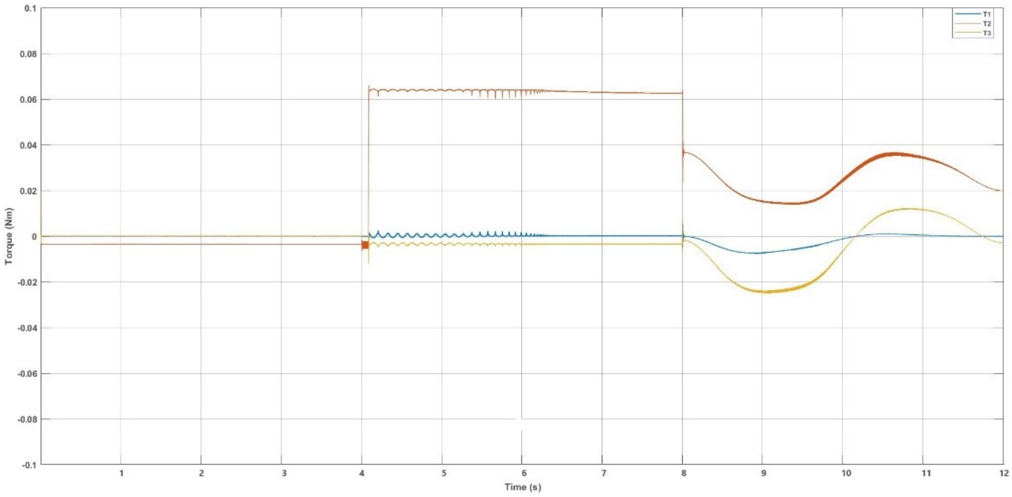

Figure 3.30: *R3 – Swing movement in the first fraction of tripod period*

3.4. Sensors

The adoption of sensors is fundamental to the realization of robotic systems that ensure high performance through integrated control. Two main types of sensors can be distinguished: intrinsic parameter sensors and extrinsic parameter sensors.

3.4.1. Intrinsic parameters sensors

Intrinsic parameter sensors measure quantities related to the internal state of the robot such as wheel speed, torques, acceleration, attitude, etc.

The robot has been equipped with an Inertial Measurement Unit (IMU), positioned on the main body, mainly used in devices to measure speed, orientation, and gravitational force. This unit consists of three accelerometers, three gyroscopes, three magnetometers and a thermometer. It can also be equipped with an extended Kalman filter to provide roll, pitch, heading and Heave, with an accuracy of 0.1° for roll and pitch, 0.8° for Heading and 5cm for Heave.

The sensors that the IMU is equipped with are used for sensor fusion and to calculate attitude angles. a desired attitude for the main body can be to remain level regardless of the terrain conformation or to make sure, on the contrary, that it is always parallel to the terrain. it is possible to compensate the position of the legs when inclinations occur, as in *fig.3.11.*

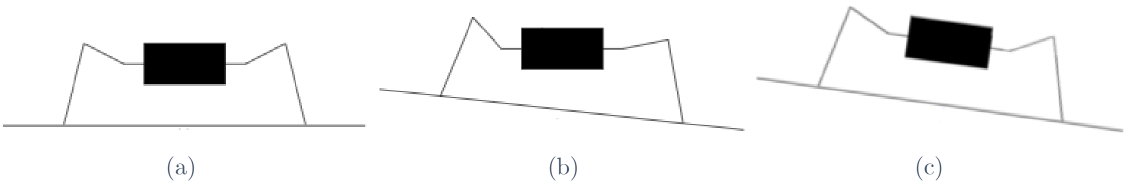
(a) (b) (c)

Figure 3.31: *Different angles of the ground and the leg positions of the hexapod*

From (a) to (b) for the hexapod to remain level, the height of the legs on both sides must be changed. Using trigonometric relations:

$$\Delta h = d - \operatorname{atan}(\alpha) \tag{13}$$

In the equation Δh is the difference in the height of a leg due to the angle of inclination of the ground, d is the distance from the center of the body to the position of the leg along the *y-axis*, and α is the angle of inclination of the ground. This Δh value is added to the z_0 coordinate of the EE of the legs for one side only, thus succeeding in leveling the main body.

From (b) to (c) it is possible to consider state (c) as state (a) with regard to leg position, the same reasoning made from (a) to (b) is applicable just by placing Δh equal to 0. [32]

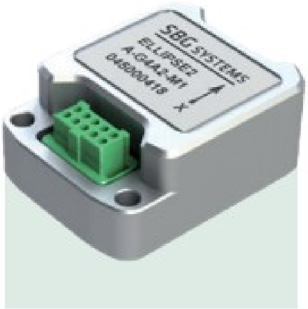

Figure 3.32: *Ellipse 2 Micro AHRS (dimensions :26.8 x 18.8 x 9.5 mm^3 ; weight : 10*

Another intrinsic parameter sensor is supplied with the servos and is responsible for measuring the angle of the joints. The servo has an angular position sensor that is a potentiometer. This sensor is a device that outputs a voltage proportional to the displacement and thus to the position taken, making it possible to perform feedback control of position or, by deriving the signal, of speed.

3.4.2. Extrinsic parameters sensors

Extrinsic parameter sensors measure quantities external to the robot, i.e., inherent to the environment in which the robot operates, and allow characterizing its interaction by increasing its autonomy. Their use allows obstacle avoidance, localization of mobile robots, and navigation in unstructured environments.

Mapping the lava tubes is the rover's first purpose; to do this, it is necessary to know the path taken by it during exploration. The camera is one of the sensors that can be used for this purpose, through algorithms Stereo Localization and Mapping (SLAM) is carried out, which has the task of reconstructing the path taken in an environment, especially an unstructured one, based on the landmarks that are captured by the camera, as well as making it possible to choose a path free from obstacles. Since the sensor chosen is a single camera for precision MonoSLAM algorithms will be used.

The camera identified is a 2MP Arducam Mini and can be well mated with Arduino boards; is dimensions are 24 x 34 mm.

As the MonoSLAM is less efficient than StereoSLAM this sensor provides the capability to add multiple cameras to a single microcontroller.

Figure 3.33: *Arducam Mini 2MP*

Chapter 4

Conclusions

Having established the possibility of using the servos identified in the construction of the robot, it is then possible to make it of the dimensions indicated above, making it compact but at the same time equipped with all the necessary tools for what is the idea of its mission. One of the main attractions of the design, and the one that led to the idea of miniaturizing it, is the possibility of being able to make a prototype using the 3D printer in the Department of Industrial Engineering.

The robot was initially conceived as a rover for exploration, but nothing precludes the use of this design, perhaps changing its analysis sensors, for search and rescue operation as well, given its small size and the possibility of making it fairly quickly because it does not need an overly large 3D printer to create the parts.

Despite being only a preliminary work, this was useful to understand the limitations of this design and how to act to upgrade the system.

In fact, with the knowledge gained during the development of this work it is possible to recognize that there are improvements that could be put into practice in the design that would make the robot more efficient. For example, one of these lies in the geometry of the arrangement of the legs: arranging them with a phase-shift angle, by making the main body octagonal instead of rectangular, would increase the freedom of movement of the legs and the maximum step. Given the speed limitations resulting from the use of these actuators, another action to improve the system might be to choose slightly larger servos, widening the system in favour of greater rover walking speed.

However, a controller would have to be added to the main model that would recognize sensor signals and process them to choose the right trajectory based on the detected obstacles, just as it would make it possible to control the robot's gait, rotation, and attitude via an external joystick.

The scripts made, then, serve as the basis for the robot's advancement but there is a need to integrate them all together for the robot to be called autonomous.

In its initial function, problems such as the difficulty of communication that would result from being underground as well as the almost total absence of light that would lead to an inability to charge the batteries would still need to be addressed.

As specified several times, this is a preliminary work based only on proving that it was possible to create a rover that was small but could still accomplish its assigned exploration mission.

Chapter 5

Bibliography

1. Grzelczyk, D., Stańczyk, B. & Awrejcewicz, J. Prototype, control system architecture and controlling of the hexapod legs with nonlinear stick-slip vibrations. *Mechatronics* 37, 63–78 (2016).
2. Tedeschi, F. & Carbone, G. Design issues for hexapod walking robotsdesign issues
3. Manoonpong, P. *et al.* Insect-inspired robots: Bridging biological and artificial systems. *Sensors* vol. 21 (2021).
4. Blamont, J. A roadmap to cave dwelling on the Moon and Mars. *Advances in Space Research* 54, 2140–2149 (2014).
5. Léveillé, R. J. & Datta, S. Lava tubes and basaltic caves as astrobiological targets on Earth and Mars: A review. *Planetary and Space Science* 58, 592–598 (2010).
6. Sauro, F. *et al.* Lava tubes on Earth, Moon and Mars: A review on their size and morphology revealed by comparative planetology. *Earth-Science Reviews* vol. 209 (2020).
7. Sawłowicz, Z. A short review of pyroducts (Lava tubes). *Annales Societatis Geologorum Poloniae* vol. 90 513–534 (2020).
8. Mars climate, important temperature difference between day and night | BIRA-IASB. https://www.aeronomie.be/en/encyclopedia/mars-climate-important-temperature-difference-between-day-and-night.
9. Deepa, T. *et al.* Design and implementation of bio inspired hexapod for exploration applications. in *Materials Today: Proceedings* vol. 37 1603–1607 (Elsevier Ltd, 2020).
10. Sun, C., Yuan, M., Li, F., Yang, Z. & Ding, X. Design and Simulation Analysis of Hexapod Bionic Spider Robot. in *Journal of Physics: Conference Series* vol. 1168 (Institute of Physics Publishing, 2019).
11. Scheda AA6082 - Aviometal. http://aviometal.com/scheda-aa6082/.
12. Overview | Adafruit PCA9685 16-Channel Servo Driver | Adafruit Learning System. https://learn.adafruit.com/16-channel-pwm-servo-driver?view=all.
13. Bishop, J. L., Quinn, R. & Dyar, M. D. What lurks in the martian rocks and soil Investigations of sulfates, phosphates, and perchlorates. Spectral

and thermal properties of perchlorate salts and implications for Mars. *American Mineralogist* 99, 1580–1592 (2014).

14. Clark, B. C. & Kounaves, S. P. Evidence for the distribution of perchlorates on Mars. *International Journal of Astrobiology* 15, 311–318 (2016).
15. Davila, A. F., Willson, D., Coates, J. D. & McKay, C. P. Perchlorate on Mars: A chemical hazard and a resource for humans. *International Journal of Astrobiology* 12, 321–325 (2013).
16. Martin, P. E. *et al.* Reevaluation of Perchlorate in Gale Crater Rocks Suggests Geologically Recent Perchlorate Addition. *Journal of Geophysical Research: Planets* 125, (2020).
17. Perchlorate - Wikipedia. https://en.wikipedia.org/wiki/Perchlorate.
18. Hassler, D. M. *et al.* Mars' surface radiation environment measured with the Mars science laboratory's curiosity rover. *Science (1979)* 343, (2014).
19. Zeitlin, C. *et al.* Overview of the Martian radiation environment experiment. *Advances in Space Research* 33, 2204–2210 (2004).
20. Townsend, L. W. Implications of the space radiation environment for human exploration in deep space. *Radiation Protection Dosimetry* 115, 44–50 (2005).
21. Tack, N. *et al.* Influence of Martian Radiation-like Conditions on the Growth of Secale cereale and Lepidium sativum. *Frontiers in Astronomy and Space Sciences* 8, (2021).
22. Boezio, M., Munini, R. & Picozza, P. Cosmic ray detection in space. *Progress in Particle and Nuclear Physics* vol. 112 (2020).
23. Axani, S. N., Frankiewicz, K. & Conrad, J. M. The CosmicWatch Desktop Muon Detector: a self-contained, pocket sized particle detector. (2018) doi:10.1088/1748-0221/13/03/P03019.
24. *The Physics Behind the CosmicWatch Desktop Muon.* (2018).
25. Gómez-Elvira, J. *et al.* REMS: The Environmental Sensor Suite for the Mars Science Laboratory Rover. *Space Sci Rev* 170, 583–640 (2012).
26. Harri, A. M. *et al.* Mars Science Laboratory relative humidity observations: Initial results. *Journal of Geophysical Research E: Planets* 119, 2132–2147 (2014).
27. Petrosyan, A. *et al.* The Martian atmospheric boundary layer. *Reviews of Geophysics* 49, (2011).
28. Pál, B., Kereszturi, Á., Forget, F. & Smith, M. D. Global seasonal variations of the near-surface relative humidity levels on present-day Mars. *Icarus* 333, 481–495 (2019).

29. Climate of Mars - Wikipedia. https://en.wikipedia.org/wiki/Climate_of_Mars.
30. Olsson, P. Martian Caves as Special Region Candidates. (Luleå University of Technology, 2018).
31. Cave Climates. https://www.nckri.org/caves/cave-climates/.
32. Thilderkvist, D. & Svensson, S. Motion Control of Hexapod Robot Using Model-Based Design. (2015).
33. 'Debei, S. Lecture notes for the Space Robotics course. (2021).
34. Deepa, T. *et al.* Design and implementation of bio inspired hexapod for exploration applications. in *Materials Today: Proceedings* vol. 37 1603–1607 (Elsevier Ltd, 2020).
35. Universitas Indonesia. Fakultas Ilmu Komputer, Institute of Electrical and Electronics Engineers. Indonesia Section, Institut Pertanian Bogor. Departamen Ilmu Komputer, Universitas Negeri Surabaya & Institute of Electrical and Electronics Engineers. *2017 International Conference on Advanced Computer Science and Information Systems (ICACSIS) : Mecure Convention Ancol, Jakarta, Indonesia, October 28th-29th , 2017,.*
36. Simulink - Simulazione e progettazione Model-Based - MATLAB & Simulink. https://it.mathworks.com/products/simulink.html.
37. Model contact between two geometries - MATLAB - MathWorks Italia. https://it.mathworks.com/help/physmod/sm/ref/spatialcontactforce.html.

Acknowledgements

A conclusione dell'elaborato vorrei dedicare qualche riga a ringraziare il mio relatore il prof. Debei che mi ha seguito, con la sua disponibilità dalla scelta dell'argomento fino alla stesura finale dell'elaborato. Grazie anche al mio correlatore ing. Chiodini per i suoi consigli e per avermi suggerito puntualmente il giusto giusto approccio e le giuste modifiche da apportare al lavoro quando ne avevo bisogno.